Magnetic field at geosynchronous orbit during high-speed stream-driven storms: Connections to the solar wind, the plasma sheet, and the outer electron radiation belt

Joseph E. Borovsky[1] and Michael H. Denton[2]

Received 19 November 2009; revised 18 January 2010; accepted 25 February 2010; published 17 August 2010.

[1] Superposed-epoch analysis is performed on magnetic field measurements from five GOES spacecraft in geosynchronous orbit during 63 high-speed stream-driven storms in 1995–2005. The field strength and the field stretching angle are examined as functions of time and local time, and these quantities are compared with the properties of the solar wind, the plasma sheet, and the outer electron radiation belt. Compression of the dayside magnetosphere coincides with an increased solar wind ram pressure commencing before the arrival of the corotating interaction region (CIR). Stretching of the nightside magnetosphere occurs in two phases: a strong-stretching phase early in the storm followed by a modest-stretching phase lasting for days. The strong-stretching phase coincides with the occurrence of the superdense plasma sheet, implying that ion pressure causes the strong stretching. This nightside strong-stretching perturbation corresponds to a ~25% contribution to Dst*. The relativistic electron flux at geosynchronous orbit has a dropout recovery temporal profile that matches the strong-stretching temporal profile; however, the number density dropout and recovery of the electron radiation belt has a profile that leads the stretching profile. A comparison of geosynchronous field strengths and magnetopause field strengths indicates that magnetopause shadowing plays a role in the radiation belt dropout. Temporal fluctuations of the geosynchronous magnetic field are examined via 1 min changes of the GOES magnetic field vectors. Fluctuation amplitudes increase at all local times at storm onset and then slowly decay during the storms. The amplitude is linearly related to the Kp, PCI, and MBI indices, except during the strong-stretching phase of the storms.

Citation: Borovsky, J. E., and M. H. Denton (2010), Magnetic field at geosynchronous orbit during high-speed stream-driven storms: Connections to the solar wind, the plasma sheet, and the outer electron radiation belt, *J. Geophys. Res.*, *115*, A08217, doi:10.1029/2009JA015116.

1. Introduction

[2] There are two major types of geomagnetic storms: coronal mass ejection (CME)-driven storms and corotating interaction (CIR)-driven storms. Because an important portion of the storms associated with a CIR is directly driven by the high-speed solar wind that follows in time the CIR, CIR-driven storms are also known as high-speed stream-driven storms. Also, the CIR itself is created by the action of the high-speed stream pushing into slower wind, as a CME sheath is created by the action of a fast CME moving into slower wind. The CIR, like the CME sheath [cf. *Gosling et al.*, 1991; *Tsurutani and Gonzalez*, 1997; Y. I. Yermolaev et al., Specific interplanetary conditions for CIR-, sheath-, and ICME-induced geomagnetic storms obtained by double superposed-epoch analysis, submitted to *Advances in Space Research*, 2010], can drive specific storm phenomena. In CME-driven storms and CIR-driven storms, various solar wind features can be associated with storm driving [cf. *Tsurutani et al.*, 1988, 1995].

[3] High-speed stream-driven storms are long-duration activations of the Earth's magnetosphere-ionosphere system. High-speed stream-driven storms (1) can produce superdense, extra hot plasma sheets that can cause anomalously high spacecraft charging in the magnetosphere [*Borovsky et al.*, 1998a; *Denton et al.*, 2006; *Denton and Borovsky*, 2009], (2) can produce high fluxes of relativistic electrons in the outer electron radiation belt that can lead to dangerous spacecraft internal charging in the magnetosphere [*Paulikas and Blake*, 1976; *Belian et al.*, 1996; *Reeves*, 1998; *Wrenn and Sims*, 1996; *Love et al.*, 2000], and (3) can produce long-duration ionospheric disturbances [e.g., *Abdu et al.*, 2006; *Prölss*, 2006; *Denton et al.*, 2009a; *Chang et al.*, 2009; *Sojka et al.*, 2009]. Unlike CME-driven storms, high-speed stream-driven storms produce only weak Dst perturbations [*Yermolaev and Yermolaev*, 2002; *Denton*

[1]Space Science and Applications, Los Alamos National Laboratory, Los Alamos, New Mexico, USA.
[2]Communication Systems, Lancaster University, Lancaster, UK.

0148-0227/10/2009JA015116

et al., 2006; *Turner et al.*, 2006, 2009; *Borovsky and Denton*, 2006]; since most storm catalogs are based on the size of the Dst perturbation, high-speed stream-driven storms are often uncataloged and as a consequence less well studied than are CME-driven storms. This has been referred to as the "Dst mistake" [*Denton et al.*, 2009b].

[4] It is important to study the two types of storms separately: CME-driven storms and high-speed stream-driven storms [*Denton et al.*, 2006; see also *Vasyliunas*, 2004; *Siscoe and Siebert*, 2006]. CME-driven and high-speed stream-driven storms give rise to different phenomena [*Denton et al.*, 2006; *Borovsky and Denton*, 2006]. One underlying cause of the different behavior of the magnetosphere in the two types of storms is the systematic difference in the Mach number of the solar wind, with CME-driven storms often occurring under low Mach number wherein the solar wind/magnetosphere coupling can drastically differ from the much more typical high Mach number conditions [*Lavraud and Borovsky*, 2008; *Borovsky et al.*, 2009].

[5] In this investigation, superposed-epoch analysis will be used. Because of the repeatable nature of high-speed stream-driven storms and their solar wind drivers, high-speed stream-driven storms are particularly amenable to superposed-epoch analysis. Superposed-epoch analysis of high-speed stream-driven storms has been successful at (1) uncovering the systematic occurrence of the extra hot plasma sheet [*Denton and Borovsky*, 2009], (2) establishing the several-day lifetimes of plasmaspheric drainage plumes [*Borovsky and Denton*, 2008], (3) uncovering the role of the superdense plasma sheet in relativistic electron dropouts and recoveries [*Borovsky and Denton*, 2009c], (4) determining that compressed slow wind is the solar wind source of the superdense plasma sheet [*Denton and Borovsky*, 2009], (5) establishing that the stormtime energization of the outer electron radiation belt is a slow heating at constant number density [*Denton et al.*, 2009c], (6) quantifying hot-plasma transport time scales into and through the magnetosphere during high-speed stream-driven storms [*Denton and Borovsky*, 2009], (7) quantifying the decay rate of the outer electron radiation belts during calms before storms [*Borovsky and Denton*, 2009b], and (8) quantifying the cold-plasma mass flow in stormtime plasmaspheric drainage plumes [*Borovsky and Denton*, 2008]. Further, through the use of superposed-epoch analysis, several systematic differences between CME-driven and high-speed stream-driven storms have been catalogued [*Denton et al.*, 2006].

[6] In this report, the magnetic field morphology of the magnetosphere for high-speed stream-driven storms is of concern. There have been prior investigations of the stormtime perturbations to the magnetic field at geosynchronous orbit [e.g., *Tsyganenko et al.*, 2003; *Huang et al.*, 2006, 2008; *Ohtani et al.*, 2007], but those investigations did not differentiate between the different types of storms.

1.1. Overview of High-Speed Stream-Driven Storms

[7] High-speed stream-driven storms arise when the Parker spiral-oriented magnetic field in high-speed streams is Russell-McPherron effective [*Crooker and Cliver*, 1994; *Mursula and Zieger*, 1996; *McPherron and Weygand*, 2006]. Under typical conditions in the declining phase of the solar cycle, the high-speed wind can drive geomagnetic activity for several days. Throughout the several days of geomagnetic activity, large-amplitude fluctuations of the interplanetary magnetic field in the high-speed wind can be turning the driving of the magnetosphere on and off on time scales of tens of minutes [*Tsurutani et al.*, 1995, 1999; *Denton et al.*, 2008; *Borovsky and Denton*, 2009a; *Borovsky*, 2010].

[8] High-speed stream-driven storms (unlike CME-driven storms) tend to be preceded by "calms before the storms" that precondition the magnetosphere for the oncoming storm [*Borovsky and Steinberg*, 2006]. The geomagnetic calms are the result of slow wind upstream of sector reversals in the solar wind being Russell-McPherron noneffective (calm) if the fast wind behind the sector reversal is Russell-McPherron effective (storm). At 1 AU, the sector reversals tend to pass the Earth in the early portion of the CIR before the stream interface passes. The calm before the storm leads to a build up of the outer plasmasphere that (1) produces a decay in the number density of the outer electron radiation belt in the days before the storm [*Borovsky and Denton*, 2009b] and (2) leads to more robust plasmaspheric drainage plumes during the storms [*Borovsky and Denton*, 2008].

[9] During the early phase of a high-speed stream-driven storm, a superdense plasma sheet may occur in the magnetosphere. The origin of this superdense plasma sheet is the higher-than-average density of the compressed slow wind in the CIR prior to the passage of the stream interface [*Denton and Borovsky*, 2009]. Also early in the storm a dropout of the number density of the outer electron radiation belt may occur [*Freeman*, 1964; *Nagai*, 1988; *Blake et al.*, 2001; *Onsager et al.*, 2002; *Green et al.*, 2004]. This dropout is linked to the occurrence of a superdense plasma sheet [*Borovsky and Denton*, 2009c]: if there is no high-density solar wind, then there is no superdense plasma sheet in the magnetosphere, and there will be no relativistic electron dropout of the outer electron radiation belt. About a half day after the number density of the outer electron radiation belt drops out, the number density suddenly recovers to a new value [*Denton et al.*, 2009c] and that value stays fixed for several days thereafter. The sudden recovery of the outer electron radiation belt density is linked to the termination of the superdense plasma sheet phase of magnetospheric activity.

[10] In the late phase of the high-speed stream-driven storm, the temperature of the outer electron radiation belt slowly increases at constant number density [*Borovsky et al.*, 1998a; *Denton et al.*, 2009c]. This modest temperature increase leads to a great increase in the fluxes of energetic electrons in the tail of the outer electron radiation belt distribution function. These are the so-called killer electrons that peak in flux several days into a high-speed stream-driven storm [*Nagai*, 1988; *Baker et al.*, 1990; *Borovsky et al.*, 1998a].

1.2. Outstanding Issues

[11] There are several outstanding scientific issues concerning high-speed stream-driven storms [cf. *Kavanagh and Denton*, 2007; *Denton et al.*, 2008]. One major topic is radiation belt evolution. A specific radiation belt evolution issue is the dropout and recovery of the outer electron radiation belt and its temporal correspondence to the occurrence of the superdense plasma sheet. The dropout could be caused (1) by pitch angle scattering of radiation belt electrons into the atmospheric loss cone by plasma waves [e.g., *Thorne and*

Kennel, 1971; *Horne and Thorne*, 1998; *Summers and Thorne*, 2003; *Sandanger et al.*, 2007] or (2) by drift losses to the magnetopause owing to distortion of the magnetosphere [e.g., *West et al.*, 1972; *Li et al.*, 1997; *Desorgher et al.*, 2000; *Bortnik et al.*, 2006; *Ohtani et al.*, 2009]. The superdense plasma sheet could cause either scenario (1) or (2): with its higher-than-normal thermal energy, the superdense plasma sheet could drive electromagnetic plasma waves that do the pitch angle scattering [e.g., *Borovsky and Denton*, 2009c; *Denton and Borovsky*, 2009], or with its higher-than-normal plasma pressure, the plasma sheet could produce an extra strong distortion of the nightside magnetosphere [e.g., *Borovsky et al.*, 1998a, Figure 18].

[12] To understand the cause of the dropouts and recovery of the outer electron radiation belt during storms, a knowledge of the time-dependent morphology of the magnetospheric magnetic field is essential. Additionally, for understanding the drifts and anisotropies of the radiation belts throughout storms, the magnetic field knowledge is essential. And finally, for fully understanding the transport of hot plasma and the formation (or not) of the ring current, this magnetic field knowledge is essential. For these reasons, the magnetic field at geosynchronous orbit is studied in this project. For the study, solar wind and magnetospheric measurements from 63 high-speed stream-driven storms in the years 1995–2007 are utilized.

[13] The solar wind driver for a high-speed stream-driven storm is a high-speed stream and the CIR ahead of it [*Burlaga and Lepping*, 1977; *Tsurutani et al.*, 2006a; *Richardson*, 2006]. Typically during the passage of the CIR, geomagnetic activity increases from a low level at the beginning of the CIR to storm levels at the end with a strong increase of geomagnetic activity associated with a magnetic sector reversal [cf. *Borovsky and Denton*, 2009c, Table 1; *Denton and Borovsky*, 2009, Table 1]. The pattern of geomagnetic activity can be very repeatable from CIR to CIR [*Denton et al.*, 2009c]. Additionally, during the declining phase of the solar cycle the high-speed stream temporal pattern can be very repeatable with the 27 day rotation of the Sun. The consistency from driver to driver and from storm to storm makes high-speed stream-driven storms ideal for study using superposed-epoch analysis [cf. *Gosling et al.*, 1978; *Richter and Luttrell*, 1986; *McPherron and Weygand*, 2006; *Denton and Borovsky*, 2008, 2009; *Borovsky and Denton*, 2009c; see also Yermolaev et al., submitted manuscript, 2010, and references therein], which will be used in this investigation.

[14] This manuscript is organized as follows. In section 2, the treatment of the GOES magnetic field data, the selection of the 63 high-speed stream-driven storms, and the superposed-epoch techniques are discussed. In section 3, the properties of the solar wind and the global magnetosphere are examined for the 63 storms via superposed-epoch analysis. In section 4, the magnetic field strength at geosynchronous orbit is examined as functions of time during the storm and local time for the 63 storms. In section 5, the stretching angle of the magnetic field at geosynchronous orbit is examined as functions of time during the storm and local time for the 63 storms. In section 6, the densities, temperatures, and pressures of the ion and electron plasma sheets at geosynchronous orbit are examined for the 63 storms and compared with the evolution of the magnetic field at geosynchronous orbit. In section 7, the relativistic electron flux, the number density, the temperature, and the specific entropy of the outer electron radiation belt at geosynchronous orbit are examined for the 63 storms and compared with the evolution of the magnetic field at geosynchronous orbit. Section 8 contains discussions about (1) the timing of the geosynchronous orbit magnetic field perturbations relative to the timing of CIR phenomenology in the solar wind and (2) the difficulties with parameterization of the geosynchronous orbit magnetic field changes in terms of upstream solar wind parameters and geomagnetic indices. The study is summarized in section 9, and the findings are itemized.

2. Data Sets and Event Selection

[15] This section contains discussions about the methods used to select and clean data, about the selection of high-speed stream-driven storms for the study, and about the superposed-epoch data analysis method that will be utilized.

2.1. GOES Geosynchronous Magnetic Field Measurements

[16] For the present study, vector magnetic field as measurements from the GOES spacecraft [*Singer et al.*, 1996] in geosynchronous orbit (6.6 RE) are used. The GOES spacecraft measures the magnetic field vector using a fluxgate magnetometer [*Dunham et al.*, 1996]. Data from the years 1995–2005 is utilized, involving five GOES satellites (GOES-8 to GOES-12). For the one spacecraft GOES-8, the magnetic field measurements are corrected by subtracting 7.22 nT from the z component magnetic field following the recommendations of *Tsyganenko et al.* [2003].

[17] The GOES magnetic field data is cleaned to eliminate magnetosheath intervals. When the dynamic pressure of the solar wind is high and the interplanetary magnetic field (IMF) is southward, the magnetopause can move drastically inward and a geosynchronous satellite on the dayside of the Earth can cross the magnetopause into the magnetosheath [e.g., *Rufenach et al.*, 1989; *McComas et al.*, 1994]. At those times, the spacecraft will not be measuring magnetospheric magnetic fields, and for the present study, it is desirable to eliminate such intervals from the data set. For geosynchronous spacecraft that carry the magnetospheric plasma analyzer (MPA) plasma instruments [*Bame et al.*, 1993], identifying the magnetosheath intervals is straightforward [e.g., *McComas et al.*, 1993]. Crossings of the MPA spacecraft into the magnetosheath are rarer for northward IMF than for southward IMF [*Suvorova et al.*, 2005]. Similarly for GOES spacecraft, unless the solar wind ram pressure is very high (>10 nPa), crossings into the magnetosheath only occur for southward IMF [cf. *Suvorova et al.*, 2005, Figure 10]. At those times, the southward IMF of the magnetosheath has an orientation opposite to the orientation of the dayside magnetospheric magnetic field. With this knowledge, magnetosheath intervals are cleaned from the GOES data set by eliminating all times when the measured magnetic field is southward. (Note that this cleaning method differs from the field twist method employed by *Borovsky et al.* [2009] to clean magnetosheath intervals out of the GOES data.)

2.2. Event Selection

[18] The 63 high-speed stream-driven storms used in the present study are a subset of the 124 recurring high-speed stream-driven storms from 1993 to 2005 utilized in previous studies [*Denton and Borovsky*, 2008, 2009; *Denton et al.*, 2009c; *Borovsky and Denton*, 2009b, 2009c]. Those 124 high-speed stream-driven storms were chosen according to the strength and duration of magnetospheric convection, ignoring the Dst perturbations during the event selection. (This is in contrast to some other superposed-epoch studies [e.g., *Miyoshi and Kataoka*, 2005; *Denton et al.*, 2006; *Zhang et al.*, 2006; *Yermolaev et al.*, 2007; *Longden et al.*, 2008], which selected high-speed stream-driven storms according to their Dst perturbations.) The 124 storms were found by using the McPherron list of solar wind stream interfaces (Robert McPherron, private communication, 2007) [*McPherron and Weygand*, 2006] and then examining temporal plots of the Kp index to identify storms following the stream interfaces. Only storms that are preceded by and/or followed by another storm 27 days earlier or later were accepted into the collection. From the original 124 storms, 21 were eliminated as being weak or short lived, leaving 93 robust high-speed stream-driven storms in 1993–2005. Magnetic field measurements from the GOES spacecraft prior to GOES-8 were not as reliable as those of GOES-8 to GOES-12 (Howard Singer, private communication, 2009), so only GOES magnetic field measurements from 1995 onward are utilized in the present study. Of the 93 storms in 1993–2005, 72 are in 1995–2005 era.

[19] The set of 93 storms ends in the year 2005. Solar wind and geomagnetic data were examined for the years 2006–2008 where 27 day repeating high-speed streams are prevalent; however, the storm driven by those streams in those years are weak in terms of their Kp signature.

[20] Of the 72 high-speed stream-driven storms in the 1995–2005 era, only 63 are utilized in the present study. As will be seen in sections 4 and 5 below, the magnetic field stretching trends have aspects that are opposite in summer and in winter owing to off magnetic equator effects of the GOES spacecraft orbit. To prevent the cancellation of magnetic field effects in superposed averages, storms that occurred in winter (November, December, and January) are not used. This eliminates nine storms from the list of 72.

2.3. Superposed Averaging

[21] Because of the repeatable nature of high-speed stream-driven storms and their solar wind drivers, high-speed stream-driven storms are particularly amenable to superposed-epoch analysis. For the superposed-epoch analysis, the choice of a trigger to set the zero epoch is crucial [cf. *Ilie et al.*, 2008; *Denton et al.*, 2009c; Yermolaev et al., submitted manuscript, 2010]. For the present study, the zero epoch is chosen to be the onset of storm levels of magnetospheric convection. For each storm, the onset time of convection (storm onset) is determined from a drop in MBI (midnight boundary index). MBI is an index created from locations of the low-latitude edge of the diffuse auroral precipitation as determined by DMSP satellite overflights, mathematically shifted to local midnight [*Gussenhoven et al.*, 1983]. MBI is a proxy for the position of the inner edge of the electron plasma sheet [*Elphic et al.*, 1999], which makes it an excellent indicator of magnetospheric convection, as is Kp [*Thomsen*, 2004], but MBI has higher time resolution than the 3 h Kp index. For each of the 93 storms, storm onset is taken to be the time at which MBI crosses the value 60.7°. The storm onset times were determined to about 30 min accuracy. Note that this trigger differs from the minimum-Dst triggers used in older investigations of high-speed stream-driven storms [*Miyoshi and Kataoka*, 2005; *Denton et al.*, 2006; *Zhang et al.*, 2006; *Longden et al.*, 2008], but this trigger is similar to the trigger chosen by *Yermolaev et al.* [2007], which was the first point corresponding to a strong decrease in Dst.

3. The 63 High-Speed Stream-Driven Storms

[22] This section presents an overview of the properties of the solar wind that drives the 63 high-speed stream-driven storms and presents an overview of the global reaction of the Earth's magnetosphere to that solar wind driver.

3.1. The Solar Wind Driver

[23] The driver for high-speed stream-driven storms is fast solar wind, which is preceded by a CIR. The first portion of the CIR that passes the Earth is compressed slow wind, and the second portion of the CIR is compressed fast wind [cf. *Siscoe et al.*, 1969; *Burlaga and Lepping*, 1977; *Richardson*, 2006]. The two portions are separated by an abrupt stream interface [cf. *Burlaga*, 1974; *Gosling et al.*, 1978; *Forsyth and Marsch*, 1999; *McPherron and Weygand*, 2006].

[24] In Figure 1 superposed-epoch averages of several solar wind parameters at Earth for the 63 high-speed stream-driven storms are plotted, with the zero epoch (vertical dashed line) being the onset of storm convection. The plot in Figure 1 extends from 3 days prior to storm onset to 4 days after onset.

[25] In Figure 1 (top), the superposed average of the solar wind speed at Earth is plotted. In the days prior to storm onset, the Earth is bathed in slow solar wind with average speeds of ~400 km/s or less. Storm onset occurs as the solar wind speed is rising at Earth and in the days after storm onset the Earth is bathed in fast wind with average speeds of ~550 km/s or greater.

[26] In the second panel of Figure 1 the superposed average of the y component (GSE) velocity of the solar wind is plotted. Note the characteristic westward ($-y$) then eastward ($+y$) perturbation of the CIR [cf. *Siscoe et al.*, 1969; *Burlaga*, 1974]. The CIR stream interface, which separates slow wind (cool, lumpy, low specific entropy) from fast wind (hot, homogeneous, high specific entropy), is typically taken to be the point of reversal from westward ($-v_y$) to eastward ($+v_y$) flow [e.g., *Gosling et al.*, 1978; *McPherron and Weygand*, 2006]. As can be seen in the second panel, in the superposed averages, the onset of the storm begins a few hours prior to the passage of the stream interface. Hence, the storm onset occurs during the passage of the compressed slow wind [see also *Borovsky and Denton*, 2009c, Table 1; *Denton and Borovsky*, 2009, Table 1].

[27] In the third panel of Figure 1 the superposed average of the magnetic field strength in the solar wind plasma is plotted. As can be seen, in the slow wind days ahead of the storm onset and in the fast wind days afterward, the field

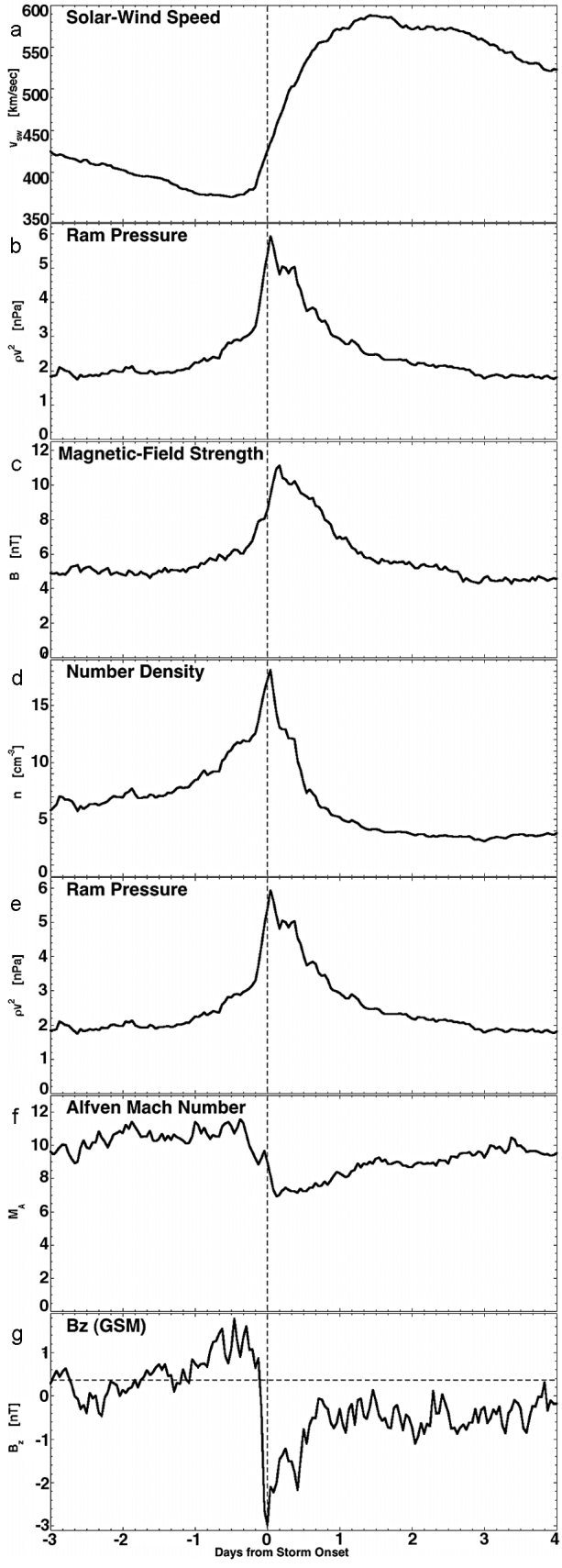

strength is similar (~5 nT). In the CIR (where the westward-eastward flow deflection is ongoing), the field is compressed, as is the solar wind plasma. In the superposed average of the solar wind magnetic field for the 63 storms, the compression is about a factor of 2 near the stream interface just after storm onset [see also *Borovsky and Denton*, 2009a].

[28] In the fourth panel of Figure 1, the number density of the solar wind plasma is plotted. The number density tends to be somewhat higher in the slow wind ahead of the CIR than in the fast wind behind [cf. *Gosling et al.*, 1978; *Richter and Luttrell*, 1986; *Richardson*, 2006; *Borovsky and Denton*, 2009a]. In the superposed averages, some of this higher density in the slow wind is owed to noncompressive high-density structures ahead of the stream interface near the sector reversal [e.g., *Gosling et al.*, 1981; *Borrini et al.*, 1981].

[29] In the fifth panel of Figure 1, the superposed average of the solar wind ram pressure ρv^2 is plotted. The temporal behavior of the ram pressure follows the temporal behavior of the solar wind plasma density (fourth panel): the ram pressure is high in the CIR because the density is high there.

[30] In the sixth panel of Figure 1, the superposed average of the Alfven Mach number $M_A = v/v_A$ of the solar wind is plotted. As can be seen, the average Mach number of the wind is high before storm onset and after storm onset. This is contrary to the case of coronal mass ejection-driven storms where the solar wind Mach number can be low [cf. *Borovsky and Denton*, 2006; *Lavraud and Borovsky*, 2008]. At low Mach number, several unusual aspects to the morphology of the stormtime magnetosphere can occur [*Lavraud and Borovsky*, 2008; *Borovsky et al.*, 2009], which makes the operation of the magnetosphere different for CME-driven storms from CIR-driven storms [*Borovsky and Denton*, 2006].

[31] In Figure 1 (bottom), the superposed average of the z component (GSM) of the solar wind magnetic field is plotted. Note that the average of B_z is positive (northward) before storm onset and negative (southward) after onset. This is caused by a sector reversal and the Russell-McPherron effect [*Russell and McPherron*, 1973]: if the Parker spiral magnetic field is Russell-McPherron effective in the fast wind after the sector reversal, then the event (a storm) may be chosen, and it follows that for chosen events (storms) the Parker spiral magnetic field prior to the sector reversal will be Russell-McPherron noneffective (a calm) [*Borovsky and Steinberg*, 2006]. Note in Figure 1 (bottom) that B_z is very strong and southward at the beginning of the

Figure 1. Using superposed averages of OMNI2 measurements, the solar wind driver for the 63 high-speed stream-driven storms is explored. The zero epoch (vertical dashed line) is the onset of storm convection. In the top, the solar wind speed is plotted. In the second panel, the transverse velocity of the solar wind is plotted. In the third panel, the solar wind magnetic field strength is plotted. In the fourth panel, the solar wind plasma number density is plotted. In the fifth panel, the solar wind ramp pressure is plotted. In the sixth panel, the Alfven Mach number of the solar wind is plotted. And in the bottom, the B_z (GSM) component of the solar wind magnetic field is plotted.

storm. This is owed to the compression of the magnetic field within the CIR, making B_z of larger amplitude. It should be noted that the plots in Figure 1 only extend to 4 days after the storm onset: high-speed stream-driven storms can persist for more than 4 days.

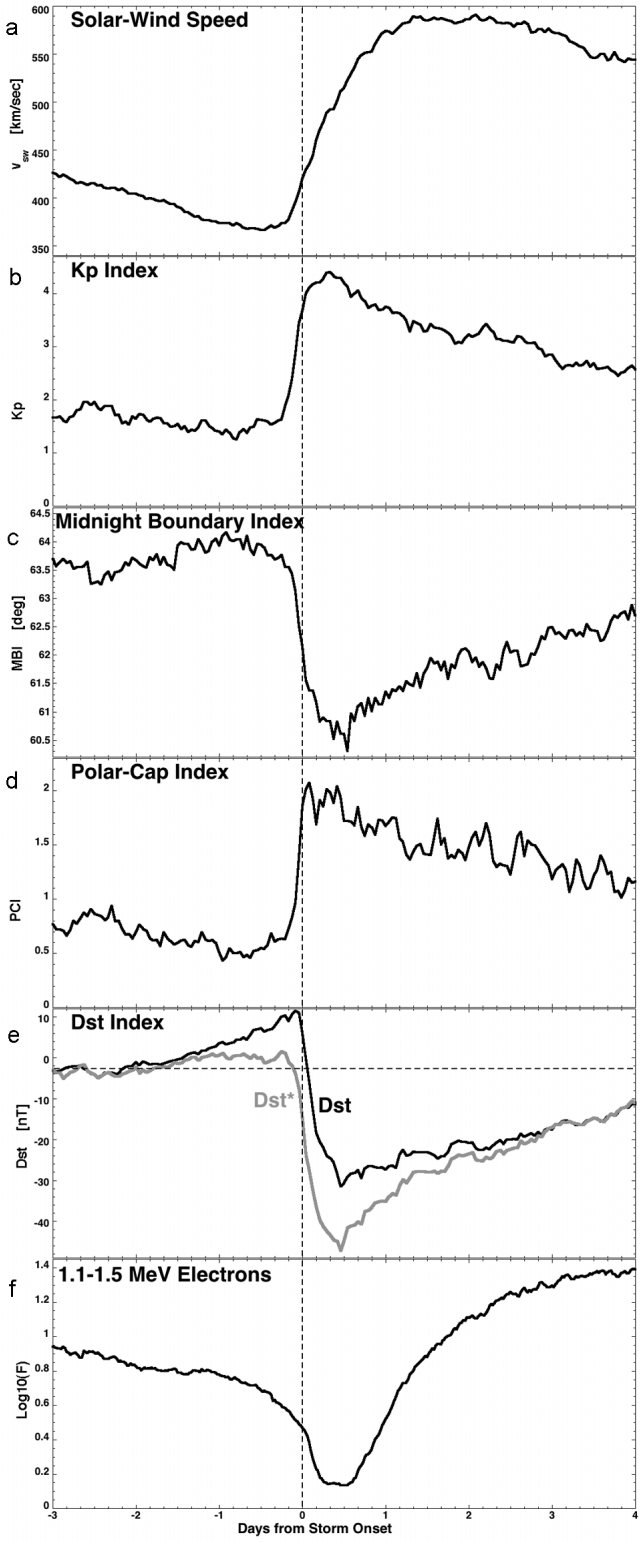

3.2. The 63 Geomagnetic Storms

[32] The reaction of the Earth's magnetosphere is displayed in the Figure 2, where superposed averages of several geomagnetic indices are plotted along with the flux of relativistic electrons at geosynchronous orbit. For reference, the superposed average of the solar wind speed is plotted in Figure 2 (top). As in Figure 1, the zero epoch (vertical dashed line) for Figure 2 is the onset of storm levels of magnetospheric convection. The plots of Figure 2 extend from 3 days prior to storm onset to 4 days after onset.

[33] In the second panel of Figure 2, the superposed average of the Kp index [*Bartels and Veldkamp*, 1949; *Rostoker*, 1972] is plotted. The Kp index is low prior to storm onset. Sometimes before a high-speed stream-driven storm there is a "calm before the storm" wherein the Kp index is near zero for a day or two [*Borovsky and Steinberg*, 2006; *Borovsky and Denton*, 2009b]. Calms before the storms contribute to the average Kp being low prior to storm onset in Figure 2. Note in the second panel that Kp rises quickly (in a fraction of a day) at storm onset and then decays slowly over several days. Note that high-speed stream-driven storms are long-duration events: the storm activity itself can last for several days [cf. *Tsurutani et al.*, 1995, 1999; *Borovsky and Denton*, 2006, 2008], as indicated by the elevated levels of Kp long after storm onset in Figure 2. The slow decline of the superposed average of Kp is owed to a slow decline of the average of the solar wind speed in the days after storm onset (see Figure 2, top).

[34] In the third panel of Figure 2, the superposed average of the Midnight Boundary Index (MBI) [*Gussenhoven et al.*, 1983] is plotted for the 63 high-speed stream-driven storms. The behavior of MBI mirrors the behavior of Kp (second panel), which is expected since MBI is a measure of the position of the inner edge of the electron plasma sheet [*Elphic et al.*, 1999], as is Kp [*Thomsen*, 2004].

[35] In the fourth panel of Figure 2 the superposed average of the polar cap index (PCI) [*Troshichev et al.*, 1988, 2000] from Thule station is plotted for the 63 high-speed stream-driven storms. PCI is a measure of the cross-polar cap current flowing in the ionosphere and is related to the cross-polar cap potential [*Troshichev et al.*, 1996; *Ridley and Kihn*, 2004]. The behavior of PCI resembles the behavior of Kp: PCI is weak and weakly decaying before the storm onset, PCI rises at storm onset, and then it decays slowly during the several days of the storm. Note in Figure 2 that the temporal trace of PCI is sharper than the trace of Kp: this is owed to the 1 h time resolution of PCI in Figure 2 and the 3 h resolution of Kp.

[36] In the fifth panel of Figure 2, the superposed average of the Dst index [*Rostoker*, 1972; *Liemohn et al.*, 2001] is plotted for the 63 high-speed stream-driven storms. Prior to

Figure 2. Superposed averages are plotted for the 63 high-speed stream-driven storms. The zero epoch (vertical dashed line) is the onset of storm convection. Plotted are the solar wind speed (top), the Kp index (second panel), MBI (third panel), PCI-Thule (fourth panel), Dst (black) and Dst* (gray) (fifth panel), and the 1.1–1.5 MeV omnidirectional electron flux at geosynchronous orbit (bottom). The electron flux is a multisatellite average using measurements at all local times.

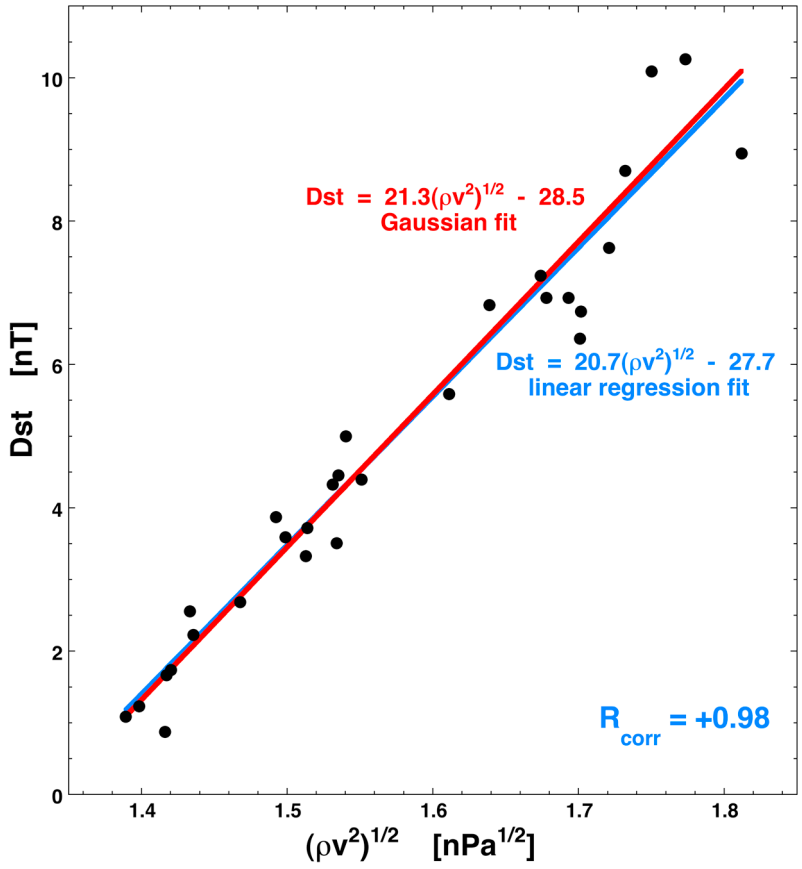

Figure 3. Hourly values of the superposed average of the Dst index for the 63 storms are plotted (black points) as a function of the superposed average of the ram pressure of the solar wind. The data are from 32 h prior to onset to 3 h prior to onset. The linear correlation coefficient is +0.98. A linear regression fit to the data appears as the blue line and a Gaussian fit to the data appears as the red line.

storm onset, Dst goes positive owing to the large increase in the ram pressure of the solar wind (cf. the fifth panel of Figure 1). At storm onset, Dst commences its move into negative values as the intensity of the storm rises. Note that for high-speed stream-driven storms strong negative values of Dst are unusual. For the 63 storms of Figure 2, the superposed average of Dst does not reach −35 nT. (But note, however, if the zero epoch would have been chosen to be the time of minimum Dst, the superposed average of Dst would have reached somewhat stronger negative values.) As is known, high-speed stream-driven storms are weak Dst makers [*Borovsky and Denton*, 2006; *Denton et al.*, 2009b]. Also plotted in the fifth panel of Figure 2 is Dst*, the value of Dst corrected for the contribution of magnetopause currents, which increase as the solar wind dynamic pressure P_{ram} increases. Dst* is given by the expression Dst* = Dst − $bP_{ram}^{1/2}$ + c [*Su and Konradi*, 1975; *Burton et al.*, 1975], where b is the change of Dst resulting from a change in $P_{ram}^{1/2}$ and c is the value of Dst on a quiet day. In the literature, a wide variety of values for (b, c) can be found, e.g., (24.1, 19.03) [*Su and Konradi*, 1975], (15.8, 20) [*Burton et al.*, 1975], (18.2, 18) [*Feldstein et al.*, 1984], (12.6, 6) [*Pudovkin et al.*, 1985], (25.32, 10.6) [*Vassiliadis et al.*, 1999], and (7.26, 11) [*O'Brien and McPherron*, 2000], where the b values are in units of nT (nPa)$^{-1/2}$ and the c values are in units of nT. We will presently contribute our more sets of (b, c) coefficients in this study. These Dst* coefficients will be derived from data fits in the time intervals just before storm onset when the magnetopause current is the dominant contribution to Dst and when a clean measurement of its effect can be obtained. The coefficients will then be used at all times to remove the effects of the magnetopause current to get a clearer view of the effects on Dst of other currents.

[37] In Figure 3, the superposed average of Dst (in units of nT) is plotted as a function of the square root of the superposed average of $P_{ram} = \rho v^2$ of the solar wind (in units of nPa) for the 63 storms; the plotted points are 1 h values over the time range from 32 h prior to storm onset, at which time the superposed average of the ram pressure of the solar wind begins to rise to 3 h prior to onset, at which time geomagnetic activity begins to overwhelm the pressure effect to turn the Dst curve toward the negative. A linear-regression fit is plotted as the blue line in Figure 3, which has the formula Dst = 20.7$P_{ram}^{1/2}$ − 27.7. This fit yields coefficients (b, c) = (20.7, 27.7). A Gaussian linear fit to the same data yields the coefficients (b, c) = (21.3, 28.5); the Gaussian fit is plotted as the red line. When the individual hourly Dst and P_{ram} values for the 63 storms are all plotted

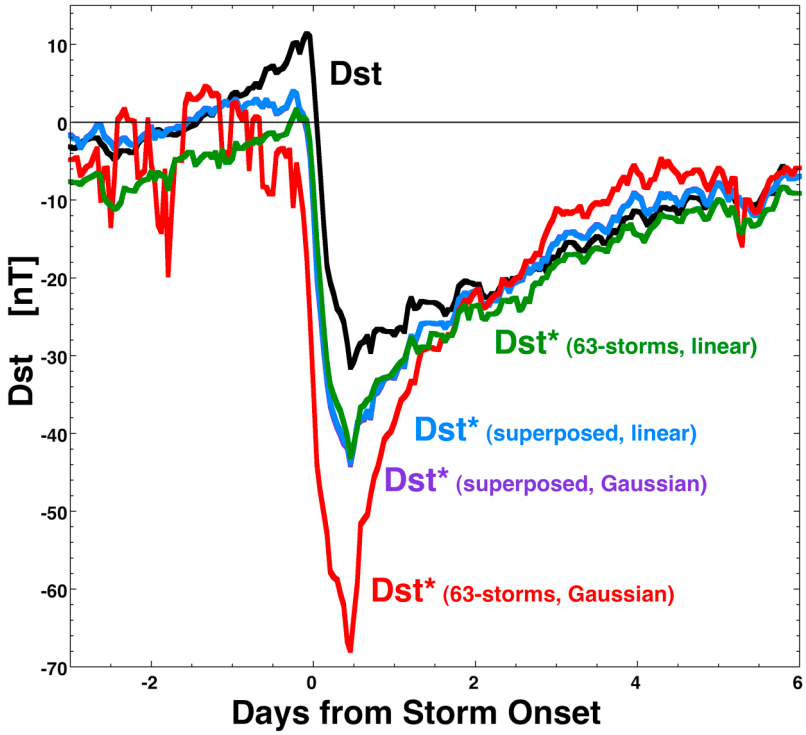

Figure 4. The superposed average of the Dst index is plotted (black) as a function of time for the 63 high-speed stream-driven storms. Using four sets of coefficients for the pressure correction to Dst, four values of Dst* are produced and plotted. The green and red curves are superposed averages of the pressure-corrected Dst, and the blue and purple curves are pressure corrections to the superposed average of Dst. The blue curve corresponds to the Dst* formula given by expressions (1).

together and fit to obtain the b and c coefficients, then the result is $(b, c) = (11.9, 14.4)$ if a linear regression fit is used and $(b, c) = (48.3, 68.6)$ if a Gaussian fit is used. These are four sets of (b, c) coefficients describing the pressure correction to Dst, yielding four manners in which to calculate Dst* from Dst. In Figure 4, the superposed average of Dst is plotted (black) as a function of time along with the four Dst* curves for the four sets of coefficients that were obtained from the 63 storm data set: the (20.7, 27.7) Dst* (blue curve) obtained from a linear-regression fit to the superposed-Dst data, the (21.3, 28.5) Dst* (purple curve) obtained from a Gaussian fit to the superposed-Dst data, the (11.9, 14.4) Dst* (green curve) obtained from a linear regression fit to the 63 storm Dst data, and the (48.3, 68.6) Dst* (red curve) obtained from a Gaussian fit to the 63 storm Dst data. As can be seen, there are substantial differences in the four Dst* curves, yielding in particular substantial differences in the minimum Dst* value of the storms. The minimum of the superposed average of Dst* ranges from −43 to −68 nT, depending on the strength of the pressure correction. Linear regression fits systematically yield the linear slopes underestimated [cf. *Borovsky et al.*, 1998b]: this results in an undercorrection for the effect of pressure on the Dst index. This is noticeable in the green curve of Figure 4, where the positive slope of Dst versus time prior to storm onset (black) still remains in the Dst* curve (green). The Gaussian fit to the data from the 63 storms yields a Dst* (red curve) that appears to overcorrect the pressure perturbation: this is seen in the red curve as the steady decrease in the value of Dst* prior to storm onset as the ram pressure of the solar wind increases. This overcorrection for pressure also produces a much deeper minimum to the Dst* curve after storm onset. The two curves (blue and purple) obtained by fitting the superposed average of Dst as a function of the superposed average of the solar wind ram pressure appear to do the best job of correctly removing the pressure perturbation prior to storm onset. The two curves are very similar: the blue curve has a smaller offset of Dst* from 0 prior to storm onset so it will be selected as the most accurate removal of the pressure perturbation from Dst. Hence, for the high-speed stream-driven storms, a pressure-corrected Dst will be taken to have the form

$$\mathrm{Dst}^{*} = \mathrm{Dst} - bP_{\mathrm{ram}}^{1/2} + c, \tag{1a}$$

$$b = 20.7\ \mathrm{nT(nPa)}^{-1/2}, \tag{1b}$$

$$c = 27.7\ \mathrm{nT}, \tag{1c}$$

where Dst* and Dst are in units of nT and $P_{\mathrm{ram}} = \rho v^2$ is in units of nPa. Using the definition of Dst* given by expressions (1), the superposed average of Dst* for the 63 storms is plotted as the gray curve in the fifth panel of Figure 2. As can be seen by examining the Dst* curve in Figure 2 (see also

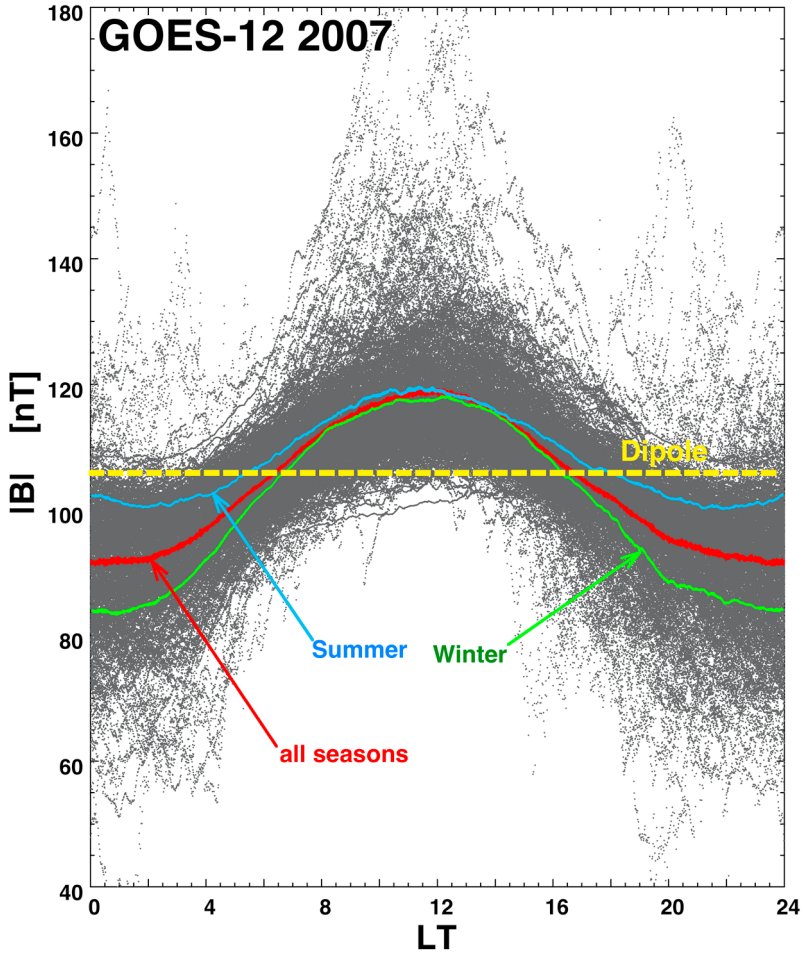

Figure 5. Using 1 min time resolution magnetic field measurements from GOES-12, the magnetic field strength at geosynchronous orbit is plotted (gray points) as a function of local time for the year 2007. The red points are 500 point running averages of the gray points. 500 point running averages are also plotted for winter-only measurements (green points) and for summer-only measurements (blue points). The nominal dipole field strength at geosynchronous orbit is plotted as the yellow dashed line.

Figure 4), in the several days after storm onset the magnitude of the Dst* perturbation slowly decreases. This has been referred to as a recovery of Dst [e.g., *Knipp et al.*, 1998; *Gonzalez et al.*, 1999; *Tsurutani et al.*, 2006b; *Turner et al.*, 2009], although its behavior is not that of a classical recovery caused by temporal decay of trapped-particle fluxes after magnetospheric driving ceases [e.g., *Dessler and Parker*, 1959; *Pudovkin et al.*, 1985]; rather, during this declining-Kp phase there is probably a balance between driving and loss of the hot plasma of the magnetosphere and that equilibrium slowly shifts as the driving of the magnetosphere slowly weakens with slowly declining solar wind speed producing the temporally weakening Dst perturbation.

[38] In Figure 2 (bottom), the superposed average of the 1.1–1.5 MeV omnidirectional electron flux at geosynchronous orbit is plotted. The flux is obtained from seven spacecrafts carrying the SOPA energetic particle detector [*Belian et al.*, 1992; *Cayton and Belian*, 2007]. Half-hour running averages of the measurements on each satellite were used to construct a multispacecraft logarithmic average (sum of log fluxes divided by number satellites) of all the available fluxes at any time [*Borovsky and Denton*, 2009b]. The multispacecraft average flux was cleaned by removing times of known solar energetic particle events and its superposed average is plotted in the Figure 2. As can be seen in Figure 2 (bottom), the geosynchronous electron flux decays in the days prior to storm onset, drops to low values at storm onset, and grows slowly and steadily in the days after storm onset. The slow decay prior to storms is owed to pitch angle scattering in a dense plasmasphere that forms during calms before the storms [cf. *Borovsky and Denton*, 2009b], the dropout (or not) at storm onset is associated with the occurrence (or not) of a superdense plasma sheet in the magnetosphere [cf. *Borovsky and Denton*, 2009c] and the steady rise in flux during the days after storm onset is associated with a slow heating of the outer electron radiation belt [*Borovsky et al.*, 1998a; *Denton et al.*, 2009c].

[39] In the following sections of this paper, more detailed looks at the reactions of the magnetospheric magnetic field morphology, the magnetospheric hot plasmas, and the outer

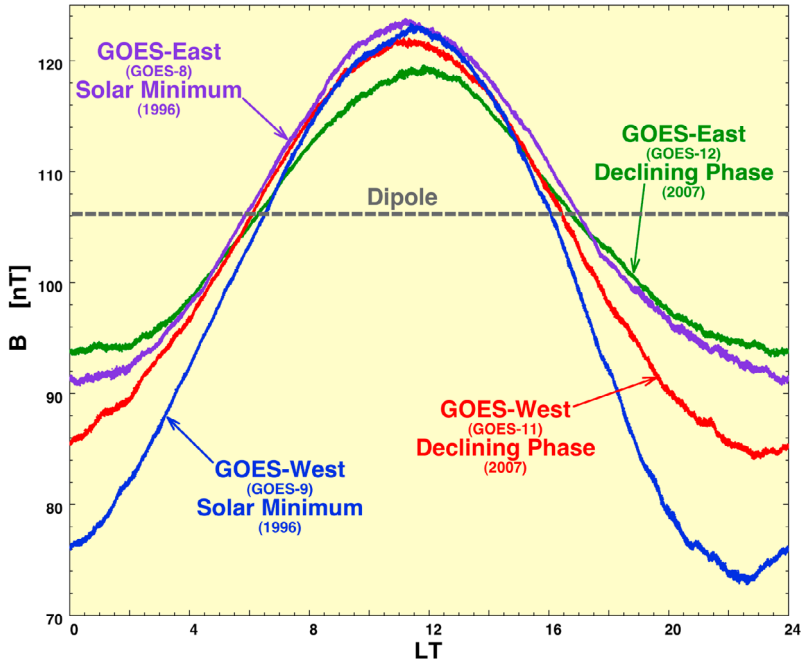

Figure 6. For two different years (1996 and 2007) and for two different GOES satellites (GOES-East and GOES-West), 500 point running averages of the magnetic field strength at geosynchronous orbit versus local time are plotted. To make the running averages, 1 min time resolution measurements were plotted versus local time. The dipole field strength at geosynchronous orbit is plotted as the dashed gray line.

electron radiation belt during these high-speed stream-driven storms will be presented.

4. Compression of the Magnetic Field During the Storms

[40] Chiefly on the dayside, the magnetic field of the Earth is known to be compressed by the solar wind to values stronger than dipole field strengths [*Hones*, 1963; *Mead*, 1964]. Exceptions are during low Mach number geomagnetic storms where dawn-to-dusk auroral zone currents can weaken the dayside magnetic field below dipole values [*Siscoe et al.*, 2004; *Borovsky et al.*, 2009].

[41] In Figure 5, the magnetic field strength at geosynchronous orbit is plotted as a function of local time for 1 year (2007) of measurements by the GOES-12 spacecraft. Individual hourly averages of the field strength are plotted in gray and a 500-point running average of the GOES-12 measurements for 2007 is plotted in red. As can be seen in the gray points, in the 1 year there is a lot of variation to the magnetic field strength at any given local time. The year 2007 was in the declining phase of the solar cycle with regular intervals of high-speed wind preceded by CIRs. The running average (red) shows the local time trend underlying the data: as can be seen in the red points, the field strength tends to be highest at about local noon and lowest at about local midnight. A nominal dipole field strength ($M_E = 7.8 \times 10^{22}$ Am^2 [*Olson and Amit*, 2006]) at geosynchronous orbit is 106 nT, as indicated by the dashed yellow horizontal line in Figure 5. As can be seen, the measured field strength tends to be higher than dipole on the dayside and lower than dipole on the nightside. Separating the measurements into a summer subset (June, July, August) and a winter subset (November, December, January), 500 point running averages are produced for summer and for winter, and these are plotted as the blue points and green points, respectively. As can be seen, there is a difference between summer and winter in the local time trend of the magnetic field strength: the nightside magnetic field strength at geosynchronous orbit is on average weaker in winter than in summer. This is owed to the fact that the GOES-12 spacecraft, which is in the geographic equator, is north of the dipole magnetic field equator; on the nightside, the hinging of the magnetotail brings GOES-12 closer to the hinged magnetic equator in winter and brings GOES-12 farther from the hinged magnetic equator in summer [*McPherron and Barfield*, 1980; *Skone et al.*, 1995].

[42] The seasonal difference in the local time trends of the field strength B (Figure 5) is not great, but as will be seen in section 5, the resulting difference in the local time trend of the stretching angle of the magnetic field will be substantial. In fact, the stretching-angle trends will be reversed from summer to winter. For this reason, in the superposed-epoch studies of the magnetospheric magnetic field in this paper, winter data (November, December, January) will be excluded and only spring, summer, and fall data will be included.

[43] Note that there are systematic differences in the local time trends seen by geosynchronous spacecraft with different longitudes [see also *McPherron and Barfield*, 1980; *Moldwin et al.*, 1998; *Ohtani et al.*, 2007]. The GOES spacecraft are located in either of two longitudes: 135°W longitude (GOES-West) or 75°W longitude (GOES-East). In Figure 6, 500 point running averages of the magnetic field strength at geosynchronous orbit are plotted for two different locations

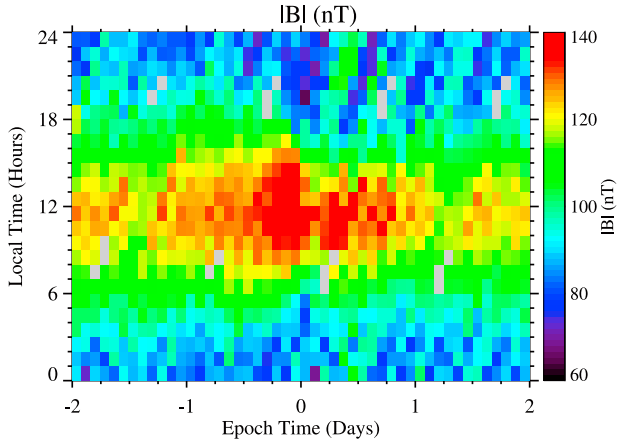

Figure 7. Using measurements from five GOES satellites during 63 high-speed stream-driven storms, the superposed average of the magnetic field strength at geosynchronous orbit (color) is plotted as a function of time from storm onset (horizontal axis) and local time (vertical axis).

(GOES-East and GOES-West) and for two different years, 1996 (solar minimum) and 2007 (declining phase). All spacecraft are located over the geographic equator, but GOES-East was more than 10° above the magnetic equator, GOES-West was closer to the magnetic equator. As can be seen in Figure 6, the spacecrafts in the GOES-West locations see deeper minima for B on the nightside. And as can be seen in the figure, the nightside minima are deeper during solar minimum than during the declining phase.

[44] In Figure 7, the superposed-epoch average of the magnetic field strength measured by GOES-8 to GOES-12 for the 63 high-speed stream-driven storms in 1995–2005 is plotted versus time (horizontal) and versus local time of observation (vertical). Time $t = 0$ in the plot is storm onset. As in Figure 5, Figure 7 shows the average magnetic field strength to be higher at local noon than on the nightside. As can be seen in Figure 7, the magnetic field strength on the dayside begins to increase about 1 day or more before the storm onset and decrease in the day after onset. On the nightside there is an indication of a weak decrease in the magnetic field strength at about the time of storm onset and a brief strengthening of the magnetic field after onset.

[45] In Figure 8, the superposed average of the magnetic field strength at geosynchronous orbit is plotted (bottom) for four local times: noon (9 LT–15 LT), dusk (15 LT–21 LT), midnight (21 LT–3 LT), and dawn (3 LT–9 LT). In Figure 8 (bottom), the four thin curves are 6 h running time averages and the four thick curves are 24 h running averages. The nominal dipole field strength at geosynchronous orbit is indicated with the horizontal dashed line. In Figure 8 (top), the superposed average of the ram pressure of the solar wind is plotted: the thin curve has a 1 h time resolution, and the thick curve is a 24 h running average. In conjunction with the increased ram pressure of the compressed solar wind in the CIR (top), the compression of the dayside magnetosphere is seen in the black curve (bottom).

[46] The increase in the dayside magnetic field strength in the magnetosphere during the CIR passage is in approximate correspondence to the change in the solar wind dynamic pressure associated with the increased solar wind plasma density in the CIR. This is shown in Figure 9 where the 24 h averaged of the superposed average of B_{mag} in the noon sector of the magnetosphere is replotted (black curve) for the 63 high-speed stream-driven storms and four mathematical expressions representing fits to magnetic field changes at geosynchronous noon as functions of solar wind ram pressure changes are plotted. The first fit (red curve in Figure 9) is the *Wing and Sibeck* [1997] equation (1) fit to B_z at geosynchronous orbit $B = C_0 + C_2(\rho v^2)^{1/2}$ with C_2 given by *Wing and Sibeck* to be $C_2 \approx 25$ nT/(nPa)$^{1/2}$ at local noon and C_0 taken to be 82 nT. The second fit (blue curve in Figure 9) is the fit from Figure 5a of *Borodkova et al.* [2006] (see also Figure 5 of *Borodkova et al.* [2008]) $B = B_o + 6.25\ \rho v^2$ with B_o taken to be the dipole value 106 nT. The third fit (green curve in Figure 9) is the fit from Figure 3a of *Villante and Piersanti* [2008] for noon $B = B_o + 27(\rho v^2)^{1/2}$ with B_o taken to be 78 nT. The fourth fit (purple) is obtained by running the T96 magnetic field model [*Tsyganenko*, 1996] for the geosynchronous equator at local noon (for March 21 with Dst = 0 and $B = 0$ in the solar wind), varying the solar wind ram pressure ρv^2 and fitting the model output: the fit $B = 103 + 7.11(\rho v^2)^{0.816}$ is obtained with B and B_o in units of nT and ρv^2 in units nPa. The four fit curves in Figure 9 approximately describe the magnitude of the increase in the magnetospheric magnetic field strength at geosynchronous orbit, with the T96 model fit being the poorest. The time profile of the increased field strength in the dayside magnetosphere (black curve in Figure 8, bottom) follows the time profile of the ram pressure of the solar wind for the compressed CIR (Figure 8, top), although the magnetospheric perturbation leads in time for the solar wind pressure perturbation as is clearly seen in Figure 9.

[47] To obtain an empirical relation between the dayside magnetic field strength B at geosynchronous orbit and the simultaneous solar wind ram pressure $P_{ram} = \rho v^2$ during the dayside compression perturbation, measurements of B and P_{ram} are extracted and fit. The data utilized are the 24 h average of the superposed average of B as measured by the GOES spacecraft within ±3 h of local noon and the 24 h average of the superposed average of ρv^2 obtained from OMNI. Data are extracted over the time interval extending from 4 days prior to storm onset to 4 days after storm onset. Simultaneous values of B and ρv^2 are the black points plotted in Figure 10. A linear regression fit to the measurements appears as the gray line in Figure 10: that fit for the magnetic field strength at geosynchronous orbit in the noon sector is

$$B = 106 + 6.3P_{ram}, \quad (2)$$

where B is in units of nT and $P_{ram} = \rho v \rho v^2$ is in units of nPa. This fit is almost exactly the same as the fit from Figure 5a of *Borodkova et al.* [2006] (blue curve in Figure 9).

[48] As can be seen by comparing the dusk (blue) and dawn (green) curves in Figure 8 (bottom), there is a dawn-dusk asymmetry to the magnetic field strength perturbation in the magnetosphere: the dusk sector shows some compression prior to the storm onset, whereas the dawn sector does not. In general, the average field strengths in the dawn and dusk sectors of geosynchronous orbit are near the dipole value (horizontal dashed line), except for the weak enhancement in the dusk sector prior to storm onset. The average field at local midnight is well below the dipole value, as seen in the red

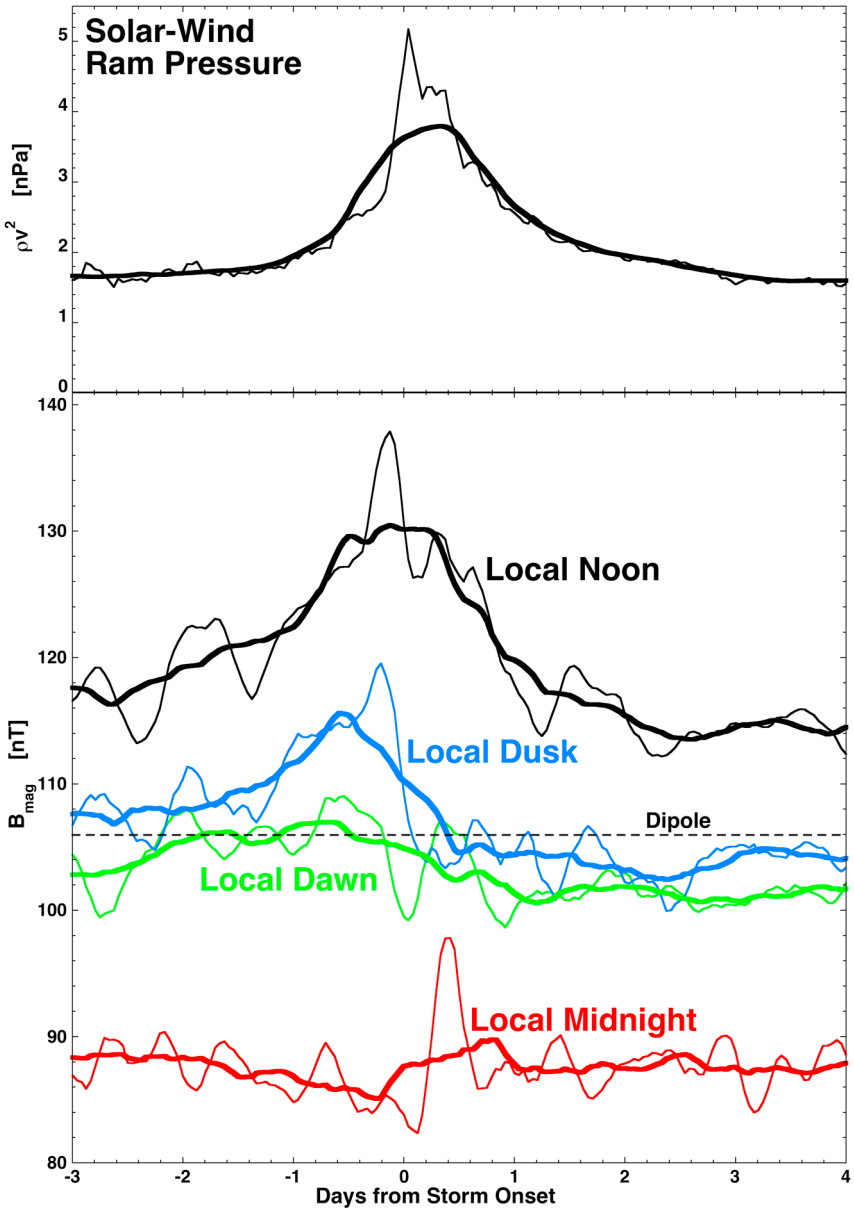

Figure 8. Superposed averages are plotted for 63 high-speed stream-driven storms. In the top, the ram pressure of the solar wind from OMNI2 measurements is plotted. In the bottom, the magnetic field strength at geosynchronous orbit as measured by five GOES satellites is plotted in the noon sector (black), the dusk sector (blue), the dawn sector (green), and the midnight sector (red). In the top, the thin curve has 1 h time resolution and the thick curve is a 24 h running average; in the bottom, the thin curves are 6 h running averages and the thick curves are 24 h running averages.

curve in Figure 8 (bottom). Note that the thin red curve (with 6 h averaging) shows an indication of the nightside field strength after storm onset and a weaker indication of a nightside field depression at storm onset. These field strength perturbations could be manifestations of strong stretching into a tail geometry.

5. Stretching of the Magnetic Field During the Storms

[49] On the nightside of the Earth, the magnetic field becomes distorted from a dipole geometry into a magnetotail geometry [*Piddington*, 1960; *Heppner et al.*, 1963] signified via the stretching angle $\theta_{stretch}$ of the field moving from dipole values ($\theta_{stretch} \sim 90°$) toward magnetotail values ($\theta_{stretch} \sim 0°$). Here the stretching angle is taken to be $\theta_{stretch} = \arctan(B_z/(B_x^2 + B_y^2)^{1/2})$ with the field components in GSM coordinates.

[50] In Figure 11, the magnetic field stretching angle $\theta_{stretch}$ at geosynchronous orbit is plotted as a function of local time for 1 year (2007) of measurements by the GOES-12 spacecraft. Individual hourly averages of the field strength are plotted in gray and a 500 point running average of the GOES-12 measurements is plotted in red. As can be seen

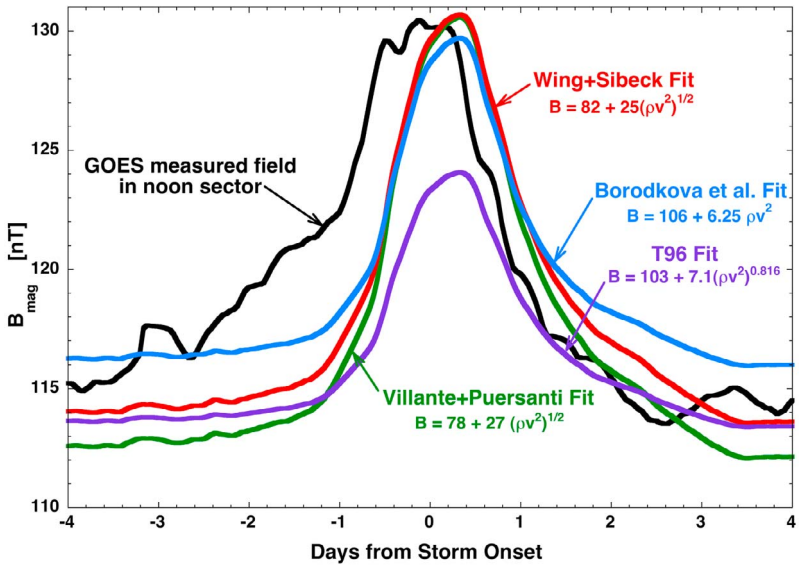

Figure 9. The 24 running average of the superposed average of the magnetic field strength in the noon sector of geosynchronous orbit as measured by five GOES spacecraft for 63 high-speed stream-driven storms is plotted as the black curve. The colored curves are plotted from various expressions for the geosynchronous orbit magnetic field strength as functions of the ram pressure of the solar wind; in the expressions the 24 h running average of the superposed average of the OMNI2 solar wind ram pressure for the 63 storms is used.

in the gray points, there is a lot of variation to the stretching angle at any given local time. The running average shows the local time trend underlying the data: as can be seen field orientation tends to be most dipolar at about local noon and can vary greatly at local midnight. Separating the 2007 measurements into a summer subset (June, July, August) and a winter subset (November, December, January), 500 point running averages are produced for summer and for winter and these are plotted as the blue points and green points, respectively, in Figure 11. As can be seen, there is a strong difference between summer and winter in the local time trend of the magnetic field stretching angle as measured by GOES-12: in summer, the stretching angles have the field dipolar on the dayside and tail-like on the nightside, but in winter, the field is more dipolar on the nightside than on the dayside. As was noted in section 4, to avoid reversals of some trends in the superposed-epoch analysis, winter data (November, December, January) will be excluded from the high-speed stream-driven storms studied in this report.

[51] In Figure 12, 500 point running averages of the stretching angle $\theta_{stretch}$ are plotted for two spacecraft (a GOES-East satellite and a GOES-West satellite) for 2 years (a solar-minimum year 1996 and a declining-phase year 2007). Note the differences in the trends between the four curves in Figure 12. The trend difference is very strong between the GOES-West (bottom two curves) and the GOES-East (top two curves) [see also *McPherron and Barfield*, 1980; *Moldwin et al.*, 1998; *Ohtani et al.*, 2007] but not so different between the solar-minimum and declining-phase curves. The measured stretch of the magnetic field away from dipole tends to be greater for the GOES-East location (off the magnetic equator) than it is for the GOES-West location (near the magnetic equator).

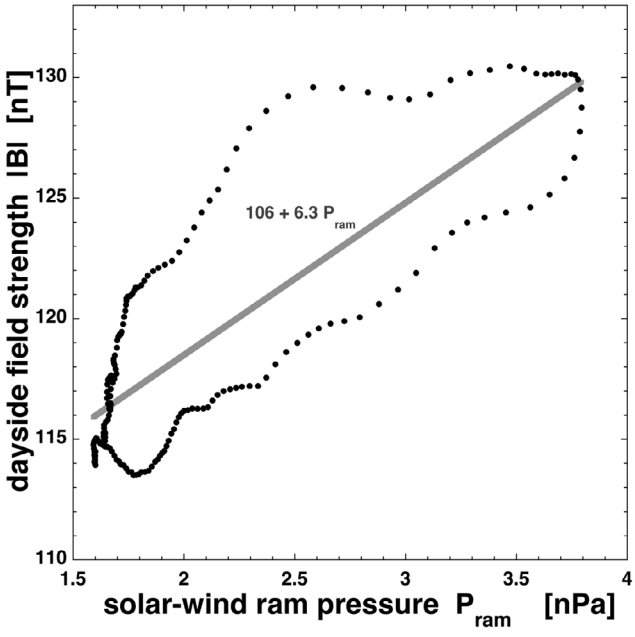

Figure 10. For the 63 high-speed stream-driven storms, the 24 h running average of the superposed average of the geosynchronous orbit magnetic field strength in the noon sector is plotted as a function of the 24 h running average of the superposed average of the solar wind ram pressure. The magnetic field is measured by five GOES satellites, and the ram pressure is from OMNI2. The points plotted are hourly data from 4 days prior to storm onset to 4 days after onset.

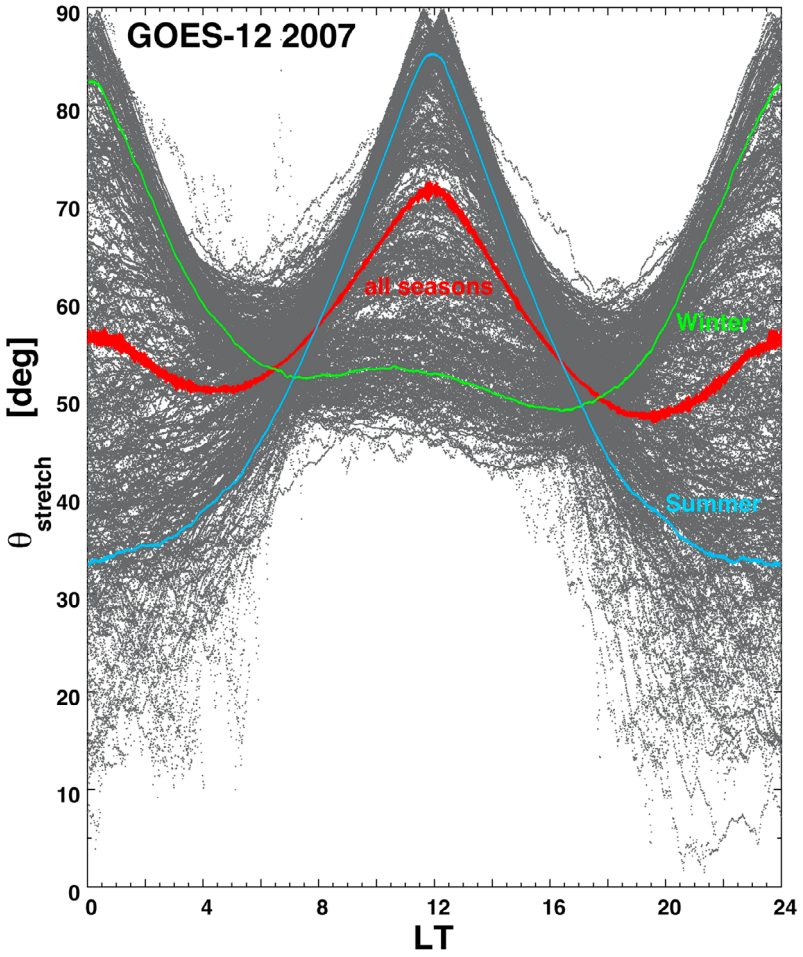

Figure 11. Using 1 min time resolution magnetic field measurements from GOES-12, the magnetic field stretching angle at geosynchronous orbit is plotted (gray points) as a function of local time for the year 2007. The red points are 500 point running averages of the gray points. 500 point running averages are also plotted for winter-only measurements (green points) and for summer-only measurements (blue points).

[52] In Figure 13, the superposed average of the magnetic field stretching angle $\theta_{stretch}$ measured by GOES-8 to GOES-12 for the 63 high-speed stream-driven storms is plotted versus time (horizontal) and local time (vertical). Time $t = 0$ is the time of storm onset. As can be seen, the field is closest to dipolar near local noon and is stretched on the nightside. There is little perturbation with time to the stretching angle on the dayside. At about the time of storm onset enhanced stretching can be seen in Figure 13 across the entire nightside.

[53] In Figure 14, the superposed average of the magnetic field stretching angle $\theta_{stretch}$ is plotted for four local times: noon (9 LT–15 LT), dusk (15 LT–21 LT), midnight (21 LT–3 LT), and dawn (3 LT–9 LT). In Figure 14 (bottom), the four thin curves are 6 h running time averages and the four thick curves are 24 h running averages. The black curves in Figure 14 show that the orientation of the dayside magnetic field at geosynchronous orbit changes little through the high-speed stream-driven storm. However, the magnetic field in the dawn (green), dusk (blue), and midnight (red) sectors undergoes stretching. In the superposed average, the stretching begins about 12 h prior to the onset of the storm (see thin curves). Often this is the onset of weak activity prior to the magnetosphere reaching storm levels of convection. A guess would be that sector reversals in the slow wind upstream of the CIR stream interface produce mildly geoeffective intervals. In the superposed averages, the midnight sector stretching reaches its peak almost 12 h after the storm onset. Note that the stretching in the midnight sector exhibits two phases: a strong-stretching phase during the first day or so of the storm followed by a long-lived modest-stretching phase where the angle slowly evolves back toward dipolar values. Comparing the blue and green curves in Figure 14, one would conclude that the change in stretching angle during the storm is about the same in the dawn sector as it is in the dusk sector, with average values of the stretching always being greater in the dawn sector (green) than in the dusk sector (blue). Note that the dawn and dusk sectors do not exhibit the two phases of stretching, they only seem to exhibit the modest-stretching phase that is long-lived. The average value of the stretching is greater still in the midnight sector (red), and the midnight sector

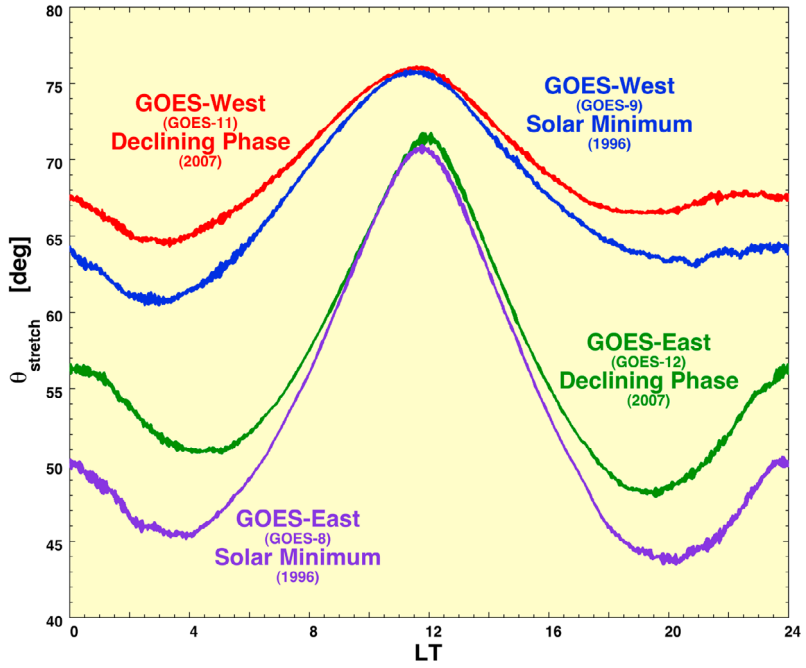

Figure 12. For two different years (1996 and 2007) and for two different GOES satellites (GOES-East and GOES-West), 500 point running averages of the magnetic field stretching angle at geosynchronous orbit versus local time are plotted. To make the running averages, 1 min time resolution measurements were plotted versus local time.

stretching perturbation associated with the storm is larger too. Comparing the thin red curve (6 h running average) with the thick red curve (24 h running average) in Figure 14, one can conclude that looking with higher time resolution will find greater amounts of stretching early in the storm.

[54] As can be discerned by examining the red curve in Figure 14, the stretched magnetic field at geosynchronous orbit on the nightside relaxes partway back toward quasi-dipole geometry by about 48 h after storm onset. Hence, the nightside stretching appears to have two phases: a strong stretching early in the storm and a milder stretching for the latter portions of the storm.

[55] In Figure 15, the temporal profile of the Dst* index is compared with the temporal profile of the stretching angle θ in the midnight sector. The superposed averages of θ (black curve, left axis) and Dst* (red curve, right axis) are plotted as functions of time for the 63 high-speed stream-driven storms. The Dst* curve is obtained from Dst via expression (1). To put both quantities on equal footing, 12 h running averages of both quantities are shown. The plot extends from 2 days before storm onset to 5 days after onset. The two-phase shape of the stretching-angle curve (black) is clearly seen, with a strong stretching phase from $t = -0.6$ days to $t = +1.0$ days and a modest-stretching phase after $t = 1.0$ days. The Dst* curve also exhibits a two-phase shape, with a "strong-stretching phase" from $t = -0.3$ days to $t = +1.2$ days and with a "modest-stretching phase" after $t = +1.2$ days. The "strong-stretching phase" of both quantities (θ and Dst*) are approximately coincidental in time. The strong-stretching phase in θ is only seen in the midnight (tail) sector (see Figure 14): we hypothesize that the strong-stretching phase in Dst* is associated with the contribution of tail currents to the Dst index. For the two curves (Dst* and θ), the decay portions of the strong-stretching phase and the decay portions of the modest-stretching phase are fit with lines: these fits are shown as the two green dashed lines for θ and the two red dashed lines for Dst*. The slopes of the linear fits are indicated in Figure 14. As can be seen, for θ the ratio of the slopes (strong decay versus modest decay) is about 14 whereas for Dst* the ratio of the slopes is only

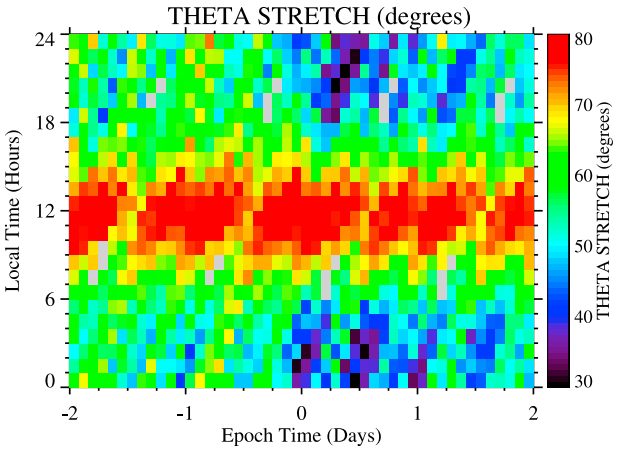

Figure 13. Using measurements from five GOES satellites during 63 high-speed stream-driven storms, the superposed average of the magnetic field stretching angle at geosynchronous orbit (color) is plotted as a function of time from storm onset (horizontal axis) and local time (vertical axis).

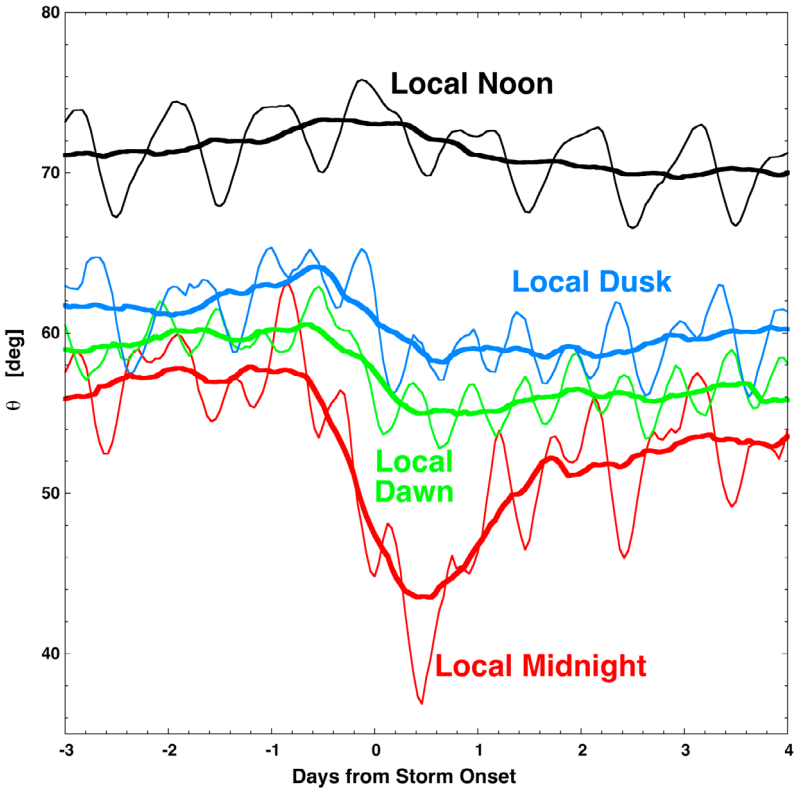

Figure 14. Superposed averages are plotted for 63 high-speed stream-driven storms. The magnetic field stretching angle at geosynchronous orbit as measured by five GOES satellites is plotted in the noon sector (black), the dusk sector (blue), the dawn sector (green), and the midnight sector (red). The thin curves are 6 h running averages and the thick curves are 24 h running averages.

about 3, indicating that the strong-stretching phase is more robust for θ than it is for Dst*.

[56] To get a measure of what fraction of Dst* is owed to tail currents, the linear fits for the modest-stretching decay of Dst* are subtracted off of Dst* at all times and the results are called Dst^*_{tail} for the four Dst* curves. These four Dst^*_{tail} curves are plotted in Figure 16 (top). As can be seen, depending on the coefficients used to correct Dst for solar wind ram pressure, various estimates are obtained of how strong the tail current contribution to Dst is for high-speed stream-driven storms. This is because the tail current phase (the strong-stretching phase) of a high-speed stream-driven storm occurs at a time when the solar wind ram pressure is high, and the resulting Dst* depends on the strength of that correction. Examining the blue curve in Figures 16 (top) and 15, without the subtraction, the peak negative value is Dst* = −43 nT and, with the subtraction, the peak negative value is Dst^*_{tail} = −9 nT. Hence, the "strong-stretching" contribution to Dst* is 9/43 ≈ 21% of the value of Dst. To determine the fractional contribution of the tail current to Dst*, the four Dst^*_{tail} curves in Figure 16 (top) are divided by the original Dst* curves and the resulting four ratios are plotted (in percent) in Figure 16 (bottom). The peak values of the ratios are indicated for each curve. As can be seen, depending on the coefficients used to make Dst* from Dst, the estimate differs. For the four sets of coefficients used, the estimated fraction of Dst* that is owed to tail currents varies from 15% to 37% for high-speed stream-driven storms. The 15% estimate comes from a Dst* that definitely has an undercorrection for the pressure (see the green curve in Figure 4 with a positive slope in Dst* prior to storm onset). The 37% estimate comes from a Dst* that probably has an overcorrection for the pressure (see the red curve in Figure 4). The blue curve in the Figure 16 (bottom), which is generated with the Dst* given by expressions (1) probably has the most accurate pressure correction: this curve yields an estimate that the tail currents contribute about 22% to the Dst* index for high-speed stream-driven storms. This 20%–25% value agrees with some previous estimates for storms [e.g., *Turner et al.*, 2000; *Ohtani et al.*, 2001] and the full range of 15%–37% values are less than other previous estimates for storms [e.g., *Alexeev et al.*, 1996; *Alexeev and Feldstein*, 2001; *Skoug et al.*, 2003; *Kalegaev et al.*, 2005; *Kalegaev and Makarenkov*, 2008]. Note, however, that most other estimates pertain to CME-driven storms.

6. Hot Plasma During the Storms

[57] To discern the connection between the hot plasma in the magnetosphere and the behavior of the magnetospheric magnetic field during high-speed stream-driven storms, MPA measurements [*Bame et al.*, 1993] of the plasmas at geosynchronous orbit are examined for the same 63 storms that were examined in sections 4 and 5 and the temporal

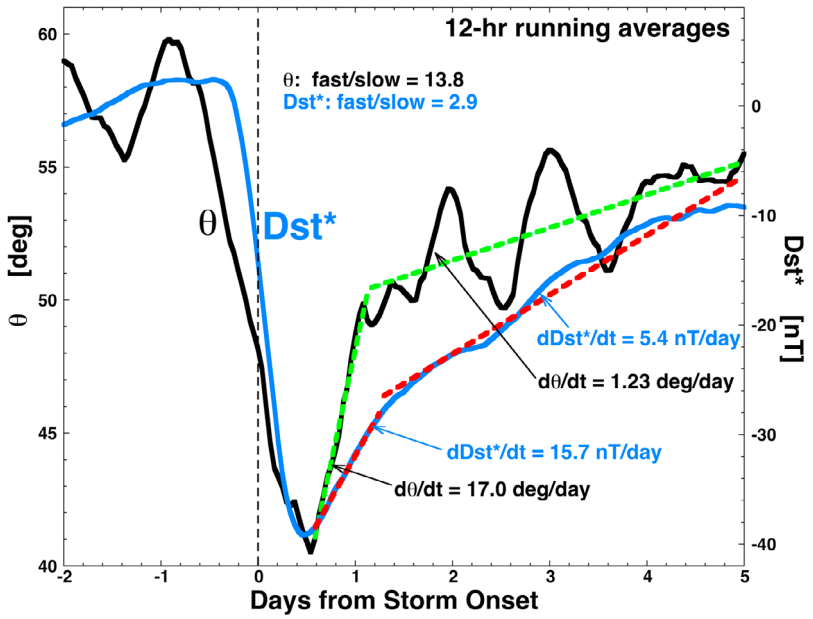

Figure 15. For the 63 high-speed stream-driven storms the temporal profile of the Dst* index is compared with the temporal profile of nightside stretching. The 12 h running average of the superposed average of the magnetic field stretching angle θ in the midnight sector of geosynchronous orbit as measured by five GOES satellites is plotted (black curve, left axis) as a function of time from storm onset. The 12 h running average of the superposed average of Dst* (20.7, 27.7) (from expression (1)) is also plotted (blue curve, right axis). For the two curves, linear regression fits to their fast-decay portions and their slow-decay portions are plotted as the line segments. The slopes of the line segments are indicated. The time of storm onset is indicated by the vertical dashed line.

behavior of the magnetic field is compared with the temporal behavior of the hot plasma.

[58] In Figure 17, the superposed average of the hot ion density, temperature, and pressure (left column) and of the hot electron density, temperature, and pressure (right column) are plotted as functions of time during the storms (horizontal axis) and local time (vertical axis). The zero epoch in the plots of Figure 17 is the time of storm onset. As can be seen, the superdense plasma sheet (top row) commences prior to storm onset and lasts about 1 day [cf. *Denton and Borovsky*, 2009] and the extra hot plasma sheet (second row) commences near storm onset and lasts for several days [cf. *Denton and Borovsky*, 2009]. As can be discerned, the superdense plasma sheet is strongest on the nightside and weaker on the dayside.

[59] In Figure 18, the superposed average of the stretching angle θ of the magnetic field at geosynchronous orbit on the nightside (20–3 LT) as measured by the GOES spacecraft for the 63 storms is plotted (black curve, left axis) as a function of time during the storm. The zero epoch of the plot (vertical dashed line) is storm onset. Also plotted in Figure 18 is the superposed average of the particle pressure of the ion plasma sheet on the nightside (21–3 LT) of geosynchronous orbit (blue curve, right axis). The ion pressure is only measured in the MPA range of energies (<40 keV), and so the plotted pressure underestimates the full ion pressure by about a factor of 2 [cf. *Borovsky et al.*, 1998a]. As can be seen in Figure 18, the temporal profiles of the nightside stretching and the nightside hot ion pressure are similar. A linear regression fit of the measured stretching angle θ and the measured MPA ion pressure P_{MPA} is made for the time interval from 3 days prior to storm onset to 3 days after onset and the linear fit is

$$\theta = 68^\circ - 15.9^\circ\ P_{\mathrm{MPA}}, \tag{3}$$

where the MPA-measured ion pressure P_{MPA} is in units of nPa. Expression (3) is plotted as the dashed green curve (right axis) in Figure 18; as can be seen, this function has a time profile very similar to the time profile of the nightside stretching angle. Because the high particle pressure of the superdense ion plasma sheet and the strong stretching of the nightside magnetic field coincide in time, one suspects that the superdense plasma sheet is responsible for the enhanced stretching of the nightside magnetic field in the early phase of high-speed stream-driven storms. (Note that the superdense plasma sheet is in turn caused by the compressed high-density solar wind of the CIR [*Denton and Borovsky*, 2009].) In Figure 18, the number density of the ion plasma sheet in the midnight sector is also plotted (orange): note the time lag between the profile of the number density and the profile of the pressure. This time lag is owed to the fact that the temperature of the ion plasma sheet temporally increases across the superdense plasma sheet phase.

[60] During the declining phase of the solar cycle, it has been shown that the stretching angle of the magnetic field at geosynchronous orbit on the nightside is correlated with the ion plasma pressure in the nightside magnetosphere [*Borovsky et al.*, 1998a]. Figure 19 [after *Borovsky et al.*, 1998a, Figure 18] plots the stretching angle θ at local mid-

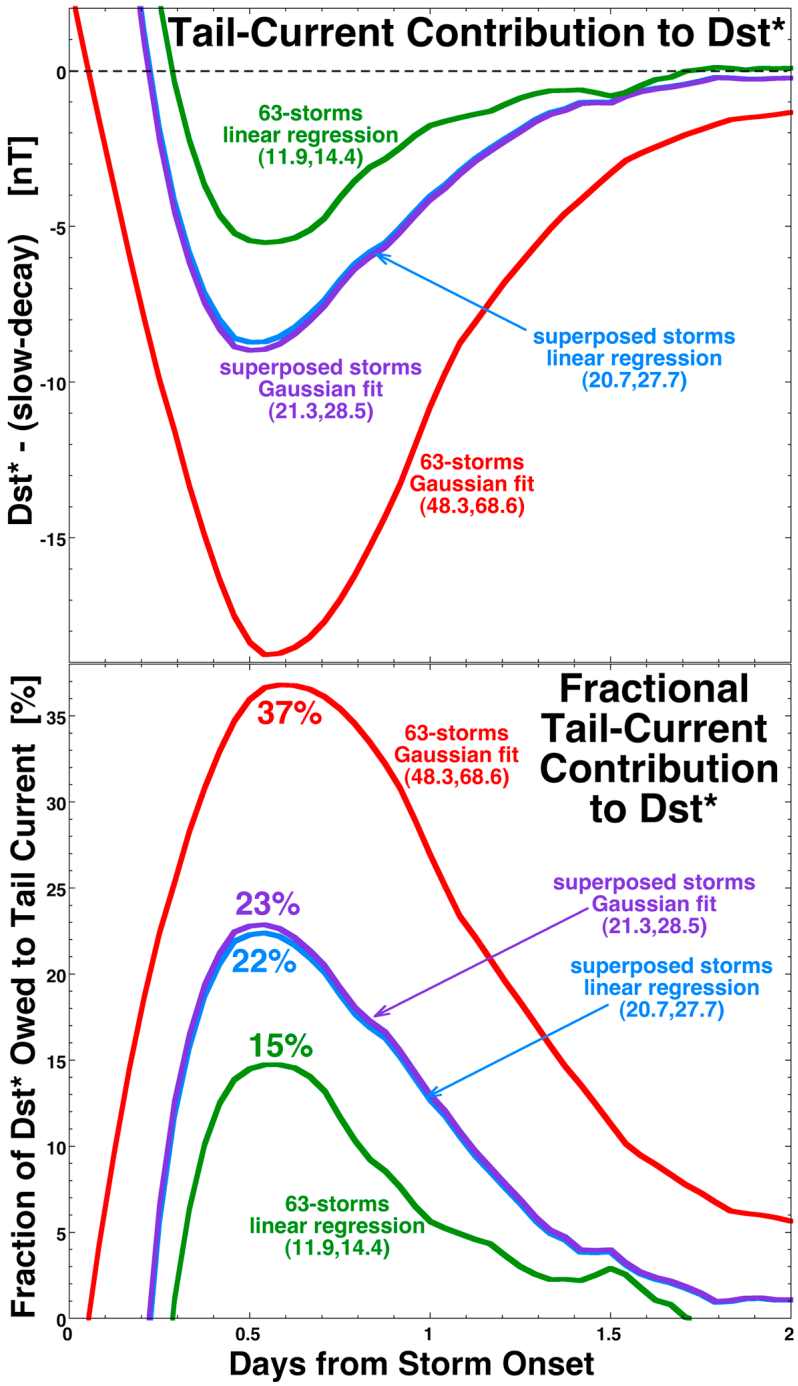

Figure 16. In the top, the slow-decay fits are subtracted from the four different Dst* curves to obtain four Dst^*_{tail} curves. In the bottom, the ratio Dst^*_{tail}/Dst^* is plotted (in percent). The peak value of the ratio during the storm is indicated for each of the four methods for obtaining Dst*. The Dst* from expression (1) is the blue curve.

night as a function of the hot ion pressure at local midnight. For Figure 19, the hot ion pressure was measured by combining MPA (0 eV to 40 keV) and Synchronous Orbit Particle Analyzer (SOPA) (50 keV to 2 MeV) measurements [*Belian et al.*, 1996; *Cayton and Belian*, 2007] of the thermal and suprathermal ions of the ion plasma sheet for the single spacecraft 1989-046 during November, December, and January of 1993–1994. This MPA-SOPA combination provides a more complete measurement of the total ion pressure than the MPA-only measurement of Figure 18. In Figure 19, the stretching angle of the magnetic field is determined from the symmetry axis of the three-dimensional ion and electron distribution functions as measured by the MPA detector [*Thomsen et al.*, 1996, 1999]. The stretching angle and the ion pressure are determined at the same time at the same location. Figure 19 plots one data point per spacecraft crossing of local

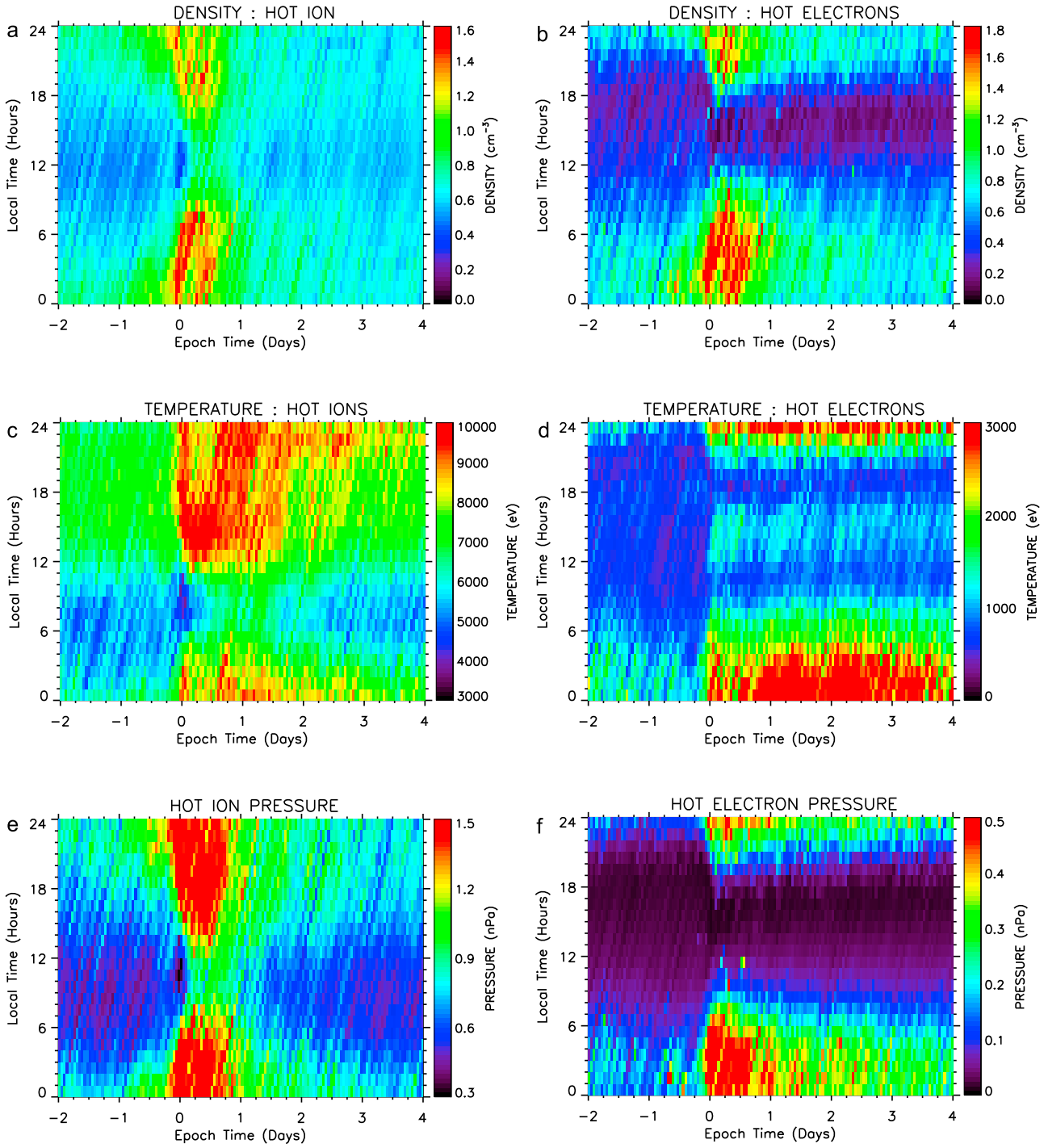

Figure 17. For 63 high-speed stream-driven storms, superposed averages of MPA measurements are plotted: in the left column, the density, temperature, and pressure of the hot ions (0.1–45 keV) around geosynchronous orbit, and in the right column, the density, temperature, and pressure of the hot electrons (0.03–45 keV) around geosynchronous orbit. In each plot, the horizontal axis is time from storm onset and the vertical axis is local time.

midnight for 3 months during which recurring high-speed stream-driven storms occurred. As can be seen, there is a definite statistical trend wherein the nightside magnetic field is more stretched (smaller θ values) when the ion pressure is higher. For the data plotted, the linear correlation coefficient between the stretching angle θ and the logarithm of the ion pressure is $R_{corr} = 0.76$. Figure 19 lends credence to the interpretation that the enhanced nightside stretching in the early portions of high-speed stream-driven storms is caused by the increased particle pressure of the superdense plasma sheet, which makes its appearance early in high-speed stream-driven storms. Earlier studies [*Denton and Borovsky*,

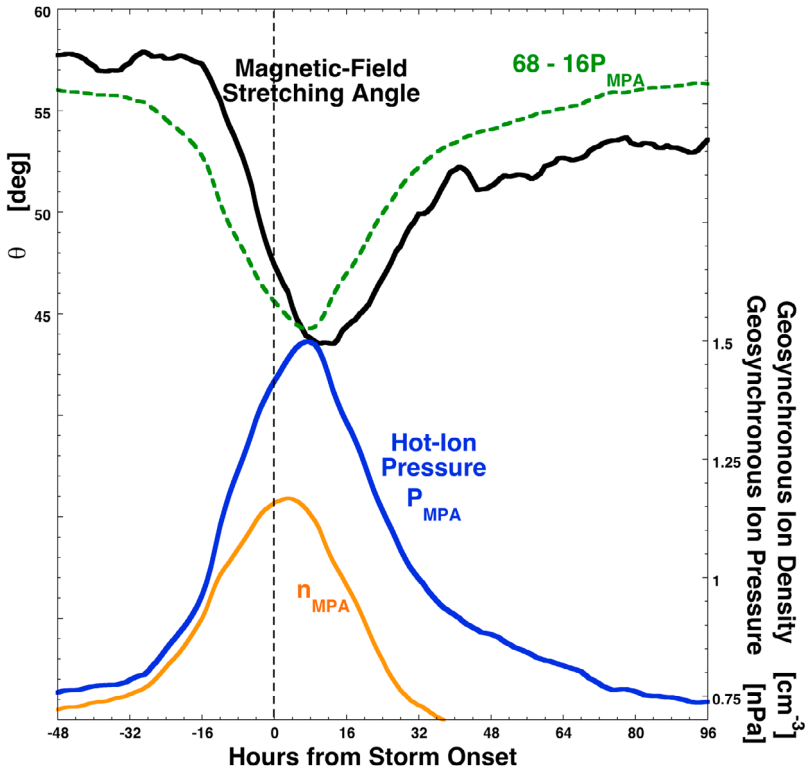

Figure 18. For the 63 high-speed stream-driven storms, the 24 h running average of the superposed average of the magnetic field stretching angle θ in the midnight sector of geosynchronous orbit as measured by five GOES satellites is plotted (black curve, left axis) as a function of time from storm onset. The superposed average of the hot ion pressure P_{MPA} in the MPA range (0–40 keV) is also plotted (blue curve, right axis), as is the hot ion density n_{MPA} (orange curve, right axis). Expression (3) is plotted in green using P_{MPA} from the blue curve.

2009] have shown that the superdense plasma sheet is owed to the compressed high-density solar wind of the CIR.

7. The Outer Electron Radiation Belt During the Storms

[61] To discern the connection between the morphology of the magnetic field at geosynchronous orbit and the dynamics of the outer electron radiation belt at geosynchronous orbit during high-speed stream-driven storms, SOPA and ESP [*Cayton et al.*, 1989; *Meier et al.*, 1996; *Cayton and Belian*, 2007] measurements of the energetic electrons at geosynchronous orbit are analyzed for the 63 storms of interest. One important phenomena that commonly occurs during high-speed stream-driven storms is the dropout of the relativistic electrons at geosynchronous orbit [*Freeman*, 1964; *Nagai*, 1988; *Borovsky et al.*, 1998a; *Blake et al.*, 2001]. This dropout occurs early in the storm and has been associated with the superdense plasma sheet [*Borovsky et al.*, 1998a; *Borovsky and Denton*, 2009c] and with magnetic field stretching at geosynchronous orbit [*Onsager et al.*, 2002, 2007; *Green et al.*, 2004].

7.1. Temporal Connections Between Radiation Belt Dynamics and Magnetic Field Evolution

[62] In Figure 20, SOPA and ESP measurements of the energetic electrons at geosynchronous orbit are used to produce superposed averages of three quantities for the 63 high-speed stream-driven storms. In Figure 20 (top), the logarithm of the omnidirectional flux of 1.1–1.5 MeV electrons is plotted. The horizontal axis is the time from storm onset, and the vertical axis is local time. As can be seen, the fluxes are systematically higher at local noon and lower on the nightside. In the days prior to storm onset the geosynchronous flux slowly decays [see also *Borovsky and Steinberg*, 2006; *Meredith et al.*, 2006; *Borovsky and Denton*, 2009b]. Near the time of storm onset, the flux decreases rapidly (onset of dropout), and the flux remains low for about 1 day. Then the flux recovers (recovery from dropout), and finally, the flux slowly increases in the several days after storm onset. Relativistic Maxwellian distributions are fit to the SOPA and ESP measurements [*Cayton et al.*, 1989; *Cayton and Belian*, 2007], yielding temperatures and densities for the radiation belt population; typical number densities of the outer electron radiation belt at geosynchronous orbit are about 4×10^{-4} cm^{-3} and typical temperatures are about 140 keV [*Denton et al.*, 2009c]. In the second and third panels of Figure 20, the superposed averages of the logarithm of the number density and of the temperature of the outer electron radiation belt at geosynchronous orbit are plotted versus time from storm onset (horizontal) and versus local time (vertical). Examining the second panel, it is seen that the number density is systematically higher on the dayside of geosynchronous orbit than

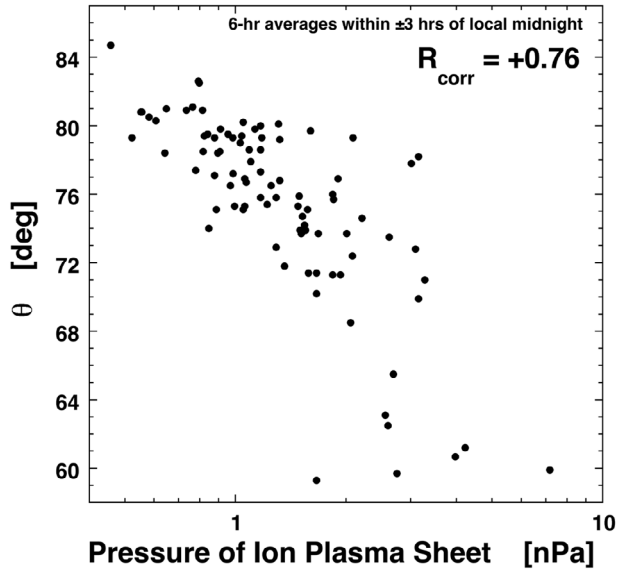

Figure 19. Using data from Figure 18 of *Borovsky et al.* [1998a], the magnetic field stretching angle θ in the midnight sector of geosynchronous orbit is plotted as a function of the MPA + SOPA ion pressure P_i in that sector. One data point is plotted per crossing of midnight (one per day) for 3 months during repeating high-speed stream-driven storms. The linear correlation coefficient between θ and $\log(P_i)$ is +0.76.

it is on the nightside. As can be seen, the number density slowly decreases with time in the days prior to storm onset, the number density drops strongly at storm onset (onset of dropout), the number density then rapidly increases (recovery from dropout) a fraction of a day after dropping out, and then the number density is approximately constant for the several days after storm onset. Examining the third panel of Figure 20, it is seen that the temperature of the outer electron radiation belt is constant in the days prior to storm onset, the temperature drops near storm onset and then increases slowly in the days following storm onset. This slow increase in the electron radiation belt temperature at fixed number density produces the steady strong increase in the relativistic electron flux during the several day long high-speed stream-driven storms [*Borovsky et al.*, 1998a].

[63] In Figure 21, the temporal evolution of the outer electron radiation belt at geosynchronous orbit is compared with the changes in the morphology of the geosynchronous magnetic field for the 63 high-speed stream-driven storms. In Figure 21 (top), the superposed average of the magnetic field strength in the noon sector of geosynchronous orbit is plotted as a function of time, with the zero epoch (vertical dashed line) being the time of storm onset. The plotted curve is a 24 h running average. The compression of the dayside magnetic field is seen as the perturbation centered in time approximately at storm onset. In the second panel of Figure 21, the superposed average of the stretching angle of the magnetic field in the midnight sector of geosynchronous orbit is plotted. The plotted curve is a 24 h running average. As can be seen, the strong-stretching phase peaks almost one half day after storm onset. In the third panel, the local time average of the superposed average of the logarithm of

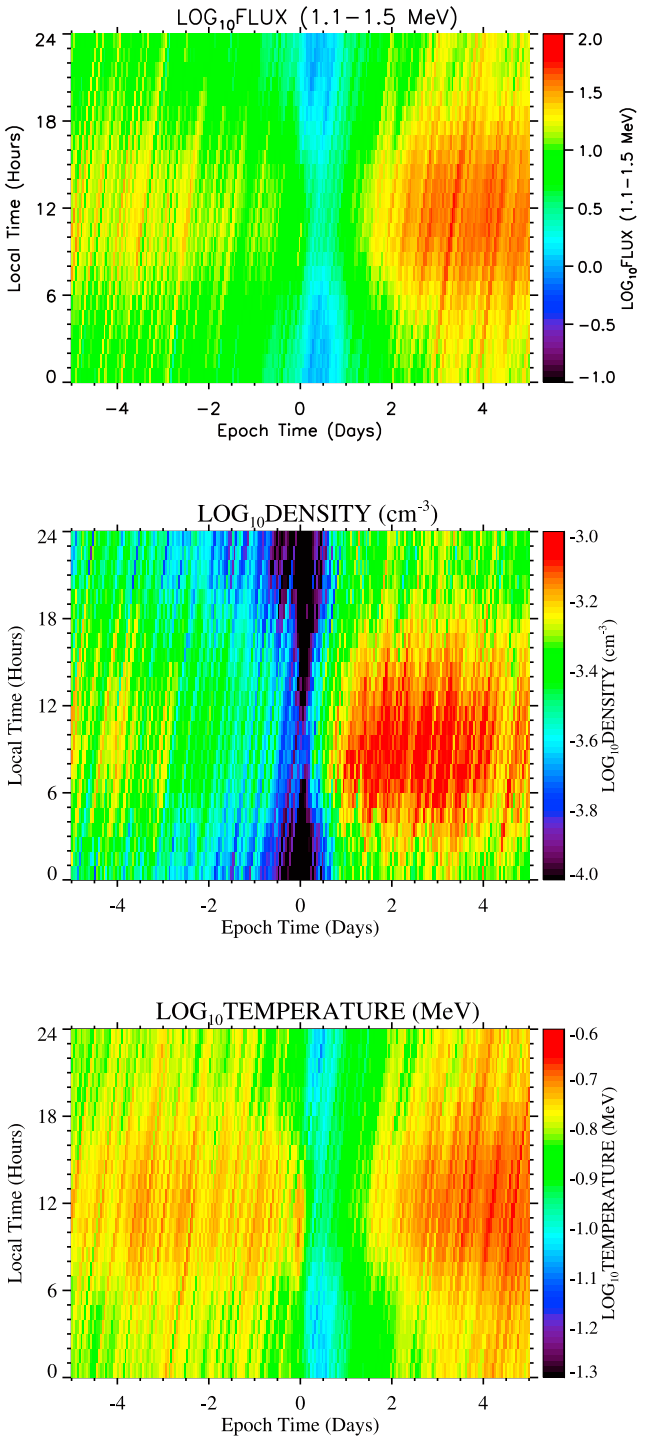

Figure 20. Using SOPA and ESP measurements at geosynchronous orbit, superposed averages of (top) the outer electron radiation belt 1.1–1.5 MeV flux, (middle) number density, and (bottom) temperature are plotted for the 63 high-speed stream-driven storms. Averaged values of these parameters at 1 hr time resolution are displayed for ±5 days from the zero epoch of convection onset. In the top, the flux units are cm^{-2} keV^{-1} $ster^{-1}$ s^{-1}.

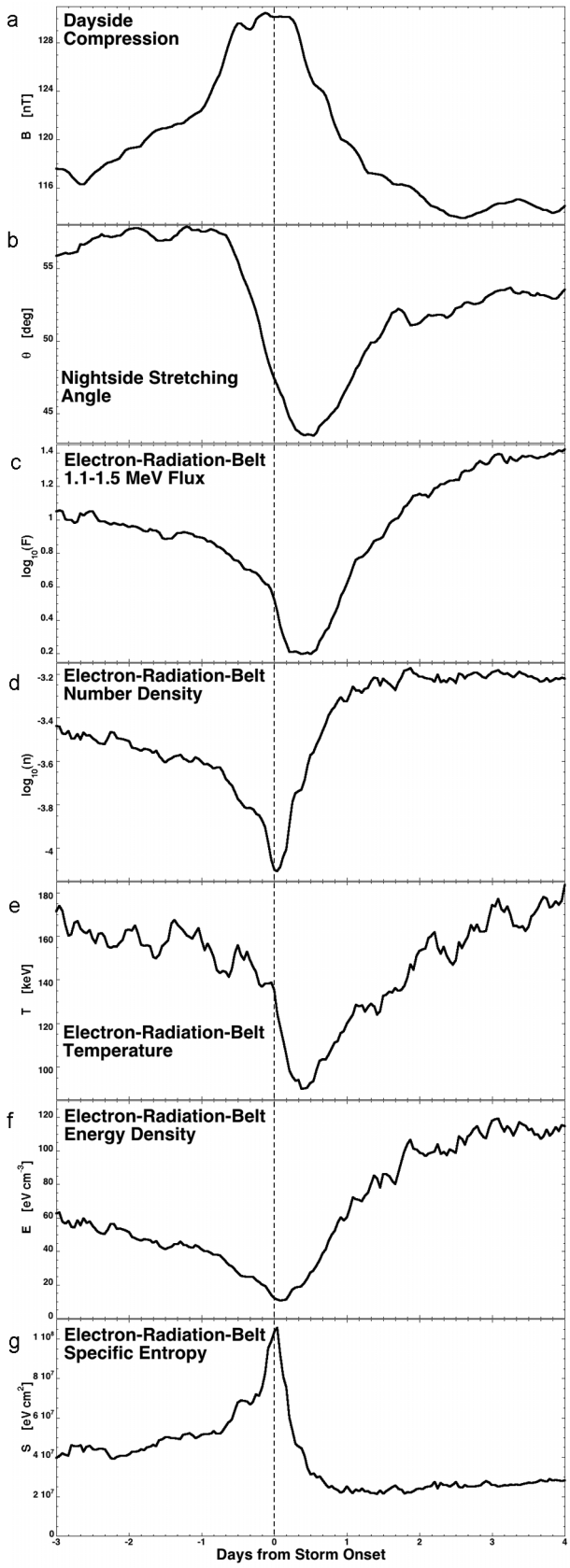

the omnidirectional flux of 1.1–1.5 MeV electrons at geosynchronous orbit is plotted. In the fourth through seventh panels of Figure 21, the local time average of the superposed averages of several quantities is plotted: the logarithm of the number density n of the outer electron radiation belt at geosynchronous orbit, the temperature T of the outer electron radiation belt at geosynchronous orbit, the energy density E ($=nk_BT$) of the outer electron radiation belt at geosynchronous orbit, and the specific entropy S ($=T/n^{2/3}$) of the outer electron radiation belt at geosynchronous orbit. As can be seen by comparing the third panel with the second panel, the temporal evolution of the relativistic electron flux resembles the temporal profile of the nightside stretching; in particular, the relativistic electron flux dropout occurs during the increase in the strong stretching and the relativistic electron flux recovery occurs as the strong stretching subsides. This temporal connection between magnetic field stretching and electron flux dropouts has been reported before [e.g., *Onsager et al.*, 2002, 2007; *Green et al.*, 2004]. The relativistic electron flux is a function of the number density of the electrons and the temperature of the electrons [*Cayton and Belian*, 2007] and the dropout of the electron flux need not be the same as the dropout of the electron density. Note in the fourth panel of Figure 21 that the dropout in the number density occurs earlier than the dropout in the flux [see also *Denton et al.*, 2009c]; the number density of the outer electron radiation belt has a dropout occurring during the beginning of the strong-stretching phase with a recovery that commences before the strong-stretching phase reaches its peak. Note also that the number density dropout fully recovers before the strong-stretching phase ends. This comparison of the temporal profile of the number density with the temporal profile of the field stretching implies that the recovery of the outer electron radiation belt from dropout is not associated with the relaxation of stretching of the magnetospheric magnetic field.

[64] In Figure 21 (bottom), the local time average of the superposed average of the specific entropy $S = T/n^{2/3}$ of the outer electron radiation belt at geosynchronous orbit is plotted. Note that the radiation belt dropout appears as a brief strong increase in the specific entropy; the strong increase in entropy is caused by a sudden drop in the density n of the outer electron radiation belt and a sudden decrease in the temperature of the outer electron radiation belt. The subsequent sudden strong drop in the specific entropy is associated with a sudden increase in the number density n of the outer electron radiation belt; this is the sudden "recovery from dropout" of the radiation belt electrons. The calcula-

Figure 21. For the 63 high-speed stream-driven storms, the superposed averages of (top) the magnetic field strength in the solar wind, (second panel) the stretching angle θ in the midnight sector of geosynchronous orbit, (third panel) logarithm of the 1.1–1.5 MeV relativistic electron flux (in units of cm^{-2} keV^{-1} s^{-1} $ster^{-1}$) at geosynchronous orbit, (fourth panel) the number density of the outer electron radiation belt at geosynchronous orbit, (fifth panel) the temperature of the outer electron radiation belt at geosynchronous orbit, (sixth panel) the energy density of the outer electron radiation belt, and (bottom) the specific entropy of the outer electron radiation belt. The black vertical dashed line is storm onset.

tion of the specific entropy $S = T/n^{2/3}$ in time series data has proven to be a powerful method of discerning different plasmas [e.g., *Burlaga et al.*, 1990; *Siscoe and Intriligator*, 1993; *Crooker et al.*, 1996; *Borovsky et al.*, 1998c; *Burton et al.*, 1999; *Osherovich et al.*, 1999; *Lazarus et al.*, 2003; *Neugebauer et al.*, 2004; *Pagel et al.*, 2004; *Borovsky*, 2008; *Johnson and Wing*, 2009]. Note in Figure 21 (bottom) that the specific entropy is different after the recovery (at about $t = +0.5$ days) than it was prior to dropout (at about $t = -1$ days): this entropy difference implies that the population of radiation belt electrons after recovery is a different population from the population before dropout [see also *Borovsky et al.*, 1998a], precluding the adiabatic "Dst effect" [e.g., *Dessler and Karplus*, 1961; *Kim and Chan*, 1997] as the cause of the dropout.

7.2. Electron Loss by Magnetopause Shadowing

[65] An outstanding issue in our attempt to understand the radiation belts is the cause of the relativistic electron dropout [*Friedel et al.*, 2002; *Kavanagh and Denton*, 2007]: specifically whether the electrons are lost to the atmosphere or to the magnetopause. *Borovsky and Denton* [2009c] found a temporal association between relativistic electron flux dropouts and the occurrence of the superdense plasma sheet in the presence of the plasmaspheric drainage plume: this association fits a scenario in which the superdense plasma sheet drives plasma waves, which scatter the radiation belt electrons into the atmospheric loss cone. On the contrary, recent calculations [*Desorgher et al.*, 2000; *Ukhorskiy et al.*, 2006; *Kim et al.*, 2008] have indicated that distortion of the magnetosphere during geomagnetic storms can cause radiation belt electrons to drift into the dayside magnetopause to be lost. And recent computer simulations have indicated that radial diffusion is important in the outer electron radiation belt [e.g., *Brautigam and Albert*, 2000; *Miyoshi et al.*, 2003; *Jordanova et al.*, 2008], which could enhance the losses to the magnetopause.

[66] In Figure 22, the possibility that the dropout is caused by the loss of radiation belt electrons to the magnetopause is explored for high-speed stream-driven storms. In Figure 22 (top), the superposed average of the logarithm of the number density of the outer electron radiation belt in the noon sector (blue) and midnight sector (red) at geosynchronous orbit is plotted as a function of time for the 63 storms, with the zero epoch (vertical dashed line) being the onset of storm convection. In the second panel, the superposed average of the logarithm of the 1.1–1.5 MeV omnidirectional electron flux in the noon sector (blue) and in the midnight sector (red) is plotted for the 63 storms. In Figure 22 (bottom), the superposed average of the magnetic field strength in the noon sector (blue) and in the midnight sector (red) of geosynchronous orbit is plotted for the 63 storms. As can be seen, the field strength at noon is stronger than the field strength at midnight. Also plotted in Figure 22 (bottom) is an estimate of the magnetic field strength at the dayside magnetopause B_{mp} at local noon. This estimate is calculated from the superposed average of the solar wind ram pressure ρv^2 (including the number density of alpha particles in the solar wind) via the pressure balance argument $K\rho v^2 = B_{mp}^2/8\pi$, where K is an aerodynamic factor accounting for the divergence of the solar wind flow near the stagnation point. Taking the high Mach number value $K = 0.88$ [*Spreiter et al.*, 1966; *Schield*, 1969], the pressure balance argument yields $B_{mp} = 47$ nT $(\rho v^2)^{1/2}$ where ρv^2 is in units of nPa. Using the superposed average of ρv^2 from the fifth panel of Figure 1, the black dashed curve in Figure 22 (bottom) is plotted.

[67] Equatorially mirroring energetic particles in the magnetosphere drift on orbits with constant magnetic field strength [*Hones*, 1963]. If the equatorial magnetic field strength on the nightside were 90 nT, then energetic electrons would drift around the Earth in an orbit where $B = 90$ nT everywhere. If the magnetic field strength at the magnetopause were 90 nT or stronger, then those nightside electrons would drift into the magnetopause on the dayside and be lost from the magnetosphere. (The depletion of particles within the magnetosphere owing to this effect is known as "magnetopause shadowing.") Owing to their off magnetic equator locations, the GOES satellites do not measure the equatorial field strength, rather they overestimate the equatorial strength. Hence, in Figure 22 (bottom), the midnight field strength at the equator is lower than ~90 nT. The magnetopause magnetic field strength (black dashed curve) in Figure 22 (bottom) begins to increase about half a day prior to storm onset and the curve crosses the 90 nT value a few hours before storm onset. A corresponding temporal behavior can be found in the decrease of the midnight number density of the outer electron radiation belt (Figure 22, top) and in the decrease of the relativistic electron flux at midnight (Figure 22, second panel). One would expect that as long as the black curve in Figure 22 (bottom) was above the red curve, the midnight density of the outer electron radiation belt should remain low since these orbits remain connected to the magnetopause. Such a behavior is seen in the midnight flux (Figure 22, second) but not in the midnight density (Figure 22, top). Hence, there is some discrepancy between the magnetopause-shadowing argument and the nightside outer electron radiation belt observations.

[68] The above argument was made for equatorially mirroring electrons (with equatorial pitch angles of 90°). For electrons at midnight with equatorial pitch angles less than 90° the affect of magnetopause shadowing is lessened. Owing to shell splitting [*Fairfield*, 1964; *Roederer*, 1967], the orbits of nightside particles with smaller pitch angles do not move out as far on the dayside as do 90° particles. It is well anticipated that magnetopause shadowing will produce characteristic features in the pitch angle distributions of nightside electrons [e.g., *West et al.*, 1973; *Fritz et al.*, 2003] since 90° electrons are more readily lost. More information about the role of magnetopause shadowing in producing the dropouts of the outer electron radiation belt during high-speed stream-driven storms awaits a future analysis of pitch angle distribution measurements with superposed-epoch techniques.

[69] There is another discrepancy between the magnetopause shadowing argument and the outer electron radiation belt observations. This discrepancy pertains to the electron observations in the noon sector. Note in the first and second panels of Figure 22 that dropouts of the number density and flux occur at noon and that these dropouts are fractionally as large as the dropouts seen at midnight and they have almost identical temporal profiles. Yet the geosynchronous satellites measuring the energetic electrons at noon are within the magnetosphere and so the orbits of these electrons are not encountering the dayside magnetopause. Hence, there is

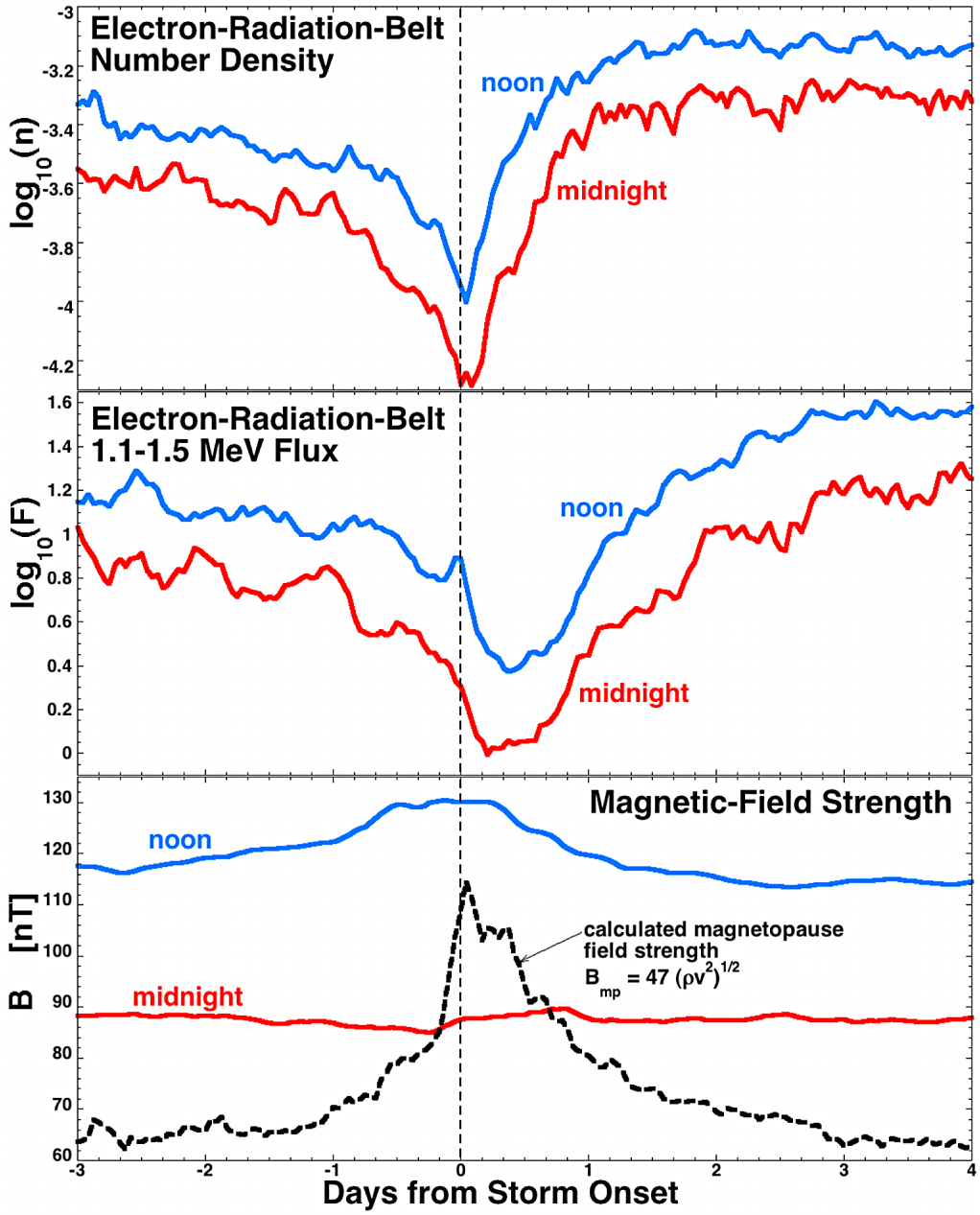

Figure 22. Superposed averages of various quantities are plotted for the 63 storms. In the top, the SOPA and ESP measurements of number density of the outer electron radiation belt at geosynchronous are plotted in the noon sector (blue) and the midnight sector (red). In the second panel, SOPA measurements of the 1.1–1.5 MeV omnidirectional electron flux at geosynchronous orbit are plotted for the noon sector (blue) and midnight sector (red). In the bottom, GOES measurements of the magnetic field strength at geosynchronous orbit are plotted for the noon sector (blue) and midnight sector (red). Also plotted is the magnetopause magnetic field strength predicted from the solar wind ram pressure.

a dropout without magnetopause shadowing and that dropout looks very much like the nightside dropout. Unless radial diffusion to the magnetopause is invoked [e.g., *Shprits et al.*, 2006], some other loss mechanism must be acting to produce the dropout. In Figure 22 (bottom), magnetic field strength at noon is plotted (blue): the value is $B > 120$ nT during the solar wind pressure pulse. In the dipolar dayside field, the GOES spacecrafts do not strongly underestimate the equatorial field strength, so $B \sim 120$ nT is probably accurate. In Figure 22 (bottom), the black dashed curve representing the calculated value of the magnetopause magnetic field strength does not reach 120 nT, but it does come within ~10% of 120 nT. Hence, at times the magnetopause could be close to geosynchronous orbit and perhaps radial diffusion to the magnetopause could be very fast and very efficient.

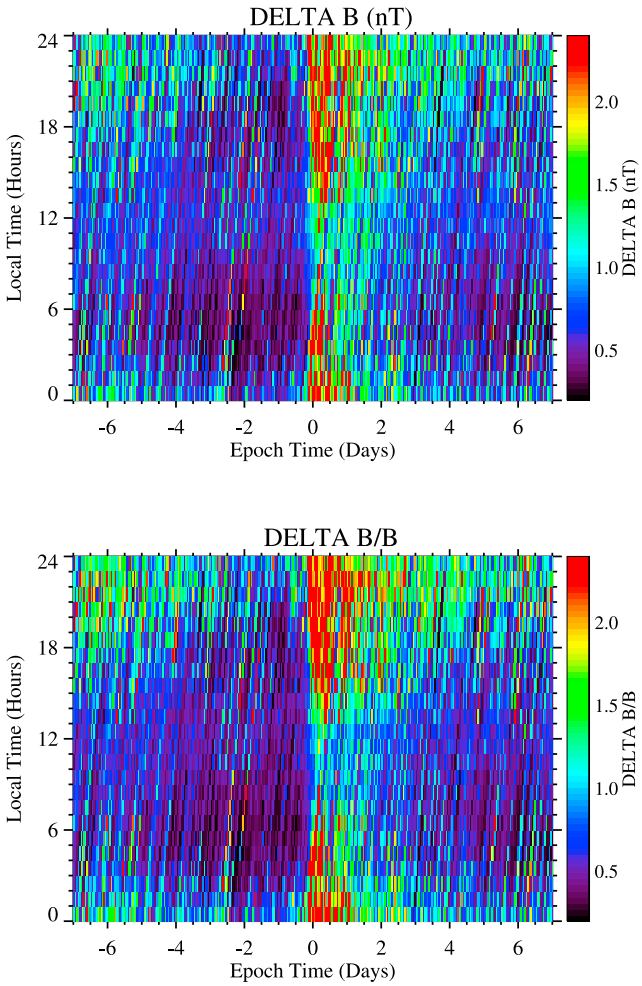

Figure 23. Using measurements from five GOES satellites during 63 high-speed stream-driven storms, the superposed average of the magnitude of the 1 min change δB of the magnetic field vector at geosynchronous orbit is plotted in the top and the superposed average of the normalized magnitude of the 1 min change $\delta B/B$ of the magnetic field vector at geosynchronous orbit is plotted in the bottom. In each panel, the horizontal axis is the time from storm onset and the vertical axis is local time).

[70] From the observations collected into Figure 22, it seems likely that magnetopause shadowing plays some role in the dropout of the outer electron radiation belt at geosynchronous orbit during high-speed stream-driven storms, although there are some discrepancies with the temporal profiles. Outstanding questions are (1) how big the role of magnetopause shadowing in producing the dropout is and (2) how the recovery operate. For these high-speed stream-driven storms, future analyses of pitch angle measurements are needed to provide further information.

8. Temporal Variations of the Geosynchronous Magnetic Field During the Storms

[71] Temporal fluctuations in the magnetic field at geosynchronous orbit are of interest for their ability to drive radial diffusion of energetic electrons in the magnetosphere [*Fälthammar*, 1965; *Perry et al.*, 2005; *Shprits et al.*, 2008] and for their ability to energize the outer electron radiation belt [*Rostoker et al.*, 1998; *Mathie and Mann*, 2000; *Elkington et al.*, 2003], which are especially relevant during high-speed stream-driven storms [*Paulikas and Blake*, 1976; *Love et al.*, 2000; *Wrenn et al.*, 2002]. In this section, 1 min changes in the magnetic field vector at geosynchronous orbit are calculated and investigated during high-speed stream-driven storms via superposed-epoch analysis. The quantity investigated is the magnitude δB of the 1 min change in the magnetic field vector δB, where $\delta B(t) = B(t + 1\ \text{min}) - B(t)$ is the 1 min change in the vector and $\delta B = |\delta B| = (\delta B_x^2 + \delta B_y^2 + \delta B_z^2)^{1/2}$ is the magnitude of the change. The normalized quantity $\delta B/B$ will also be examined, where the denominator B is the magnetic field strength. No attention will be paid to the polarization of the field changes nor to whether the changes are poloidal, toroidal, or compressive [e.g., *Saito*, 1969; *McPherron et al.*, 1972; *Orr*, 1973].

[72] In Figure 23 (top), the superposed average of δB during the 63 high-speed stream-driven storms is plotted (color) as a function of the time from storm onset (horizontal axis) and the local time of the observing GOES satellite (vertical axis). Blue indicates low levels of fluctuations (~0.5 nT over 1 min), and red indicates higher levels of fluctuations (~2.5 nT over 1 min). As can be seen, the amplitude of the magnetic field fluctuations is weak prior to storm onset and the amplitude increases suddenly at storm onset. (This increase in magnetic fluctuation amplitude at geosynchronous orbit at the onset of high-speed stream-driven storms has been reported by *Takahashi and Ukhorskiy* [2008].) As the storm progresses, the amplitude of the magnetic field fluctuations δB decreases with time. During the storm, the amplitude of δB at geosynchronous orbit is highest in the dusk sector and lowest prenoon. The dusk sector maximum of ULF power during the declining-phase geomagnetic storms has been reported in the literature [*Anderson et al.*, 1990; *Sanny et al.*, 2007].

[73] In Figure 23 (bottom), the superposed average of the normalized amplitude $\delta B/B$ of the magnetic field fluctuations during the 63 storms is plotted as functions of the time from storm onset (horizontal axis) and local time (vertical axis). The normalized amplitude $\delta B/B$ is weak before the storm, increases sharply at all local times at storm onset, and decays with time slowly during the storm. During the storm and before, the normalized amplitude is highest in the dusk-midnight sector and weakest prenoon.

[74] In Figure 24, the superposed average of the normalized amplitude $\delta B/B$ of magnetic field temporal variation at geosynchronous orbit is plotted as a function of time from storm onset. The four curves are the amplitude in the dawn sector (3–9 LT), noon sector (9–15 LT), dusk sector (15–21 LT), and the midnight sector (21–3 LT). All four curves are 12 h running averages of the superposed average. Note that the vertical axis is logarithmic. Again, it is seen that the normalized amplitude $\delta B/B$ is weak before the storm, increases rapidly at storm onset, and decays steadily as the storm progresses. Before and during the storm, the normalized amplitude $\delta B/B$ is distinctly larger in the dusk and midnight sectors than it is in the dawn and noon sectors. Note in Figure 24 that the superposed average of the amplitude $\delta B/B$ decreases steadily with time in the days

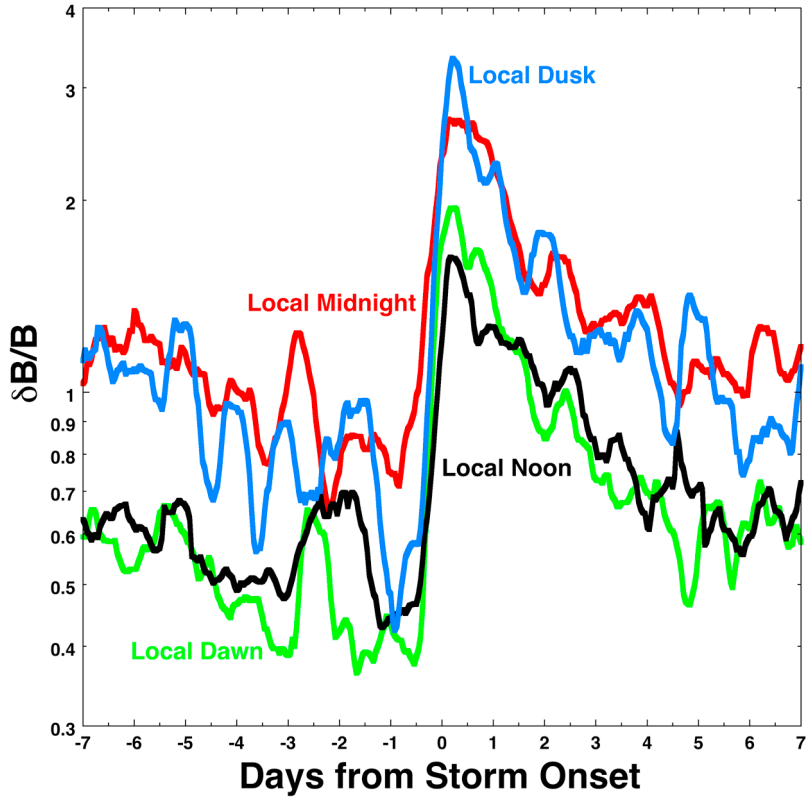

Figure 24. Using measurements from five GOES satellites during 63 high-speed stream-driven storms, 12 h running averages of the superposed average of the normalized magnitude of the 1 min change $\delta B/B$ of the magnetic field vector at geosynchronous orbit is plotted for the noon sector (black curve), the dawn sector (green curve), the midnight sector (red curve), and the dusk sector (blue curve).

before storm onset. It is believed that this decreasing amplitude is owed to the occurrence of calms before the storms [*Borovsky and Steinberg*, 2006] of varying durations, with the amplitude of $\delta B/B$ being low in each calm: closer to storm onset, the probability of being in a storm is greater.

[75] In Figure 25, the local time dependence of the superposed average of the normalized amplitude of fluctuation $\delta B/B$ is examined in detail. The black curve in Figure 25 is the average amplitude $\delta B/B$ during the day prior to the storm (averaged from time −24 h to time 0 h) plotted as a function of local time. The red curve is the average amplitude $\delta B/B$ during day 1 of the storm (from time 0 h to time 24 h), the blue curve is the average amplitude during day 2 of the storm, and the green curve is the average amplitude during day 3 of the storm. Note that the vertical axis is logarithmic. As can be seen, for each of the 4 days plotted in Figure 25 the normalized amplitude $\delta B/B$ is highest in the dusk-midnight sector and quietest in the dawn-noon sector. Note that in the day before the storm (black curve) the peak in amplitude is relatively narrow, centered at about midnight; during the storm, this peak in amplitude broadens into the dusk sector. This midnight peak during quiet times and the duskward broadening during high-speed stream-driven storms has been observed by *Sanny et al.* [2007].

[76] Note that the temporal profiles of the superposed average of the normalized amplitude $\delta B/B$ in Figure 24 resemble the temporal profiles of the Kp index and the PCI index (second and fourth panels of Figure 2). An overlay of the $\delta B/B$ curves and the index curves finds remarkable similarities in temporal behaviors for the high-speed stream-driven storms. In the three panels of Figure 26, the 12 h smoothed superposed average of $\delta B/B$ in the dusk sector (15–21 LT) is plotted as functions of three geomagnetic indices: (top) Kp, (middle) PCI, and (bottom) MBI. The plots of Figure 26 utilize hourly data points from 7 days prior to the storm onset to 7 days after onset. The linear correlation coefficients R_{corr} are indicated in each of the three panels. In the three panels linear regression fits to the data are plotted as the red lines and the linear regression formula for each line is indicated in each panel. These fits for the dusk sector $\delta B/B$ are

$$\delta B/B = 0.68\ \mathrm{Kp} - 0.50, \tag{4a}$$

$$\delta B/B = 1.31\ \mathrm{PCI} - 0.26, \tag{4b}$$

$$\delta B/B = 37 - 0.57\ \mathrm{MBI}. \tag{4c}$$

For the behavior of $\delta B/B$ before and during high-speed stream-driven storms, expressions (4) are parameterizations of the dusk sector $\delta B/B$ in terms of the three geomagnetic indices Kp, PCI, and MBI. Expressions (4) are most accurate before the storms and in the latter days of the storms. In Figure 26, data points pertaining to day 1 of the high-speed stream-driven storms are indicated in the three panels: as can

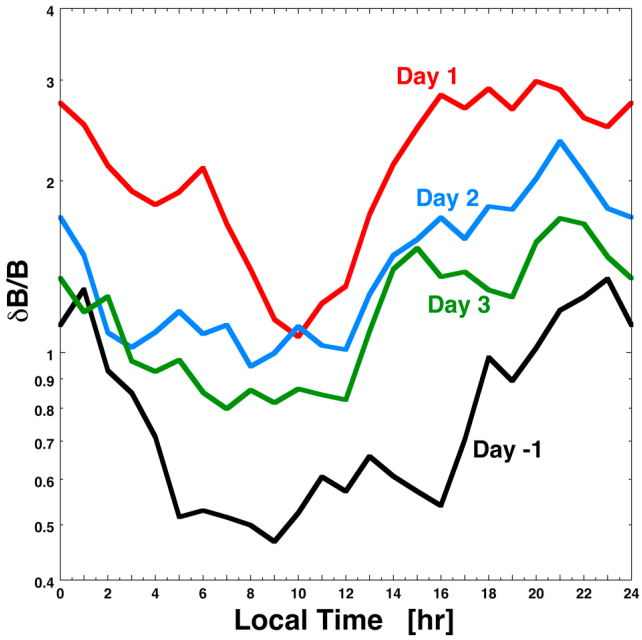

Figure 25. Using measurements from five GOES satellites during 63 high-speed stream-driven storms, 1 day averages of the superposed average of the normalized magnitude of the 1 min change $\delta B/B$ of the magnetic field vector at geosynchronous orbit is plotted as a function of local time. The black curve is the daily average for the day prior to storm onset (0–24 h prior to storm onset). The red curve is the daily average for the first day of the storm (0–24 h after storm onset). The blue curve is the daily average for the second day of the storm (24–48 h after onset). The green curve is the daily average for the third day of the storm (48–72 h after onset).

be seen, these data points deviate from the linear regression fits. These data points are from the time when the magnetic field in the nightside magnetosphere undergoes strong stretching (cf. Figure 14). Particularly noticeable in the MBI panel (bottom) of Figure 26, the data points corresponding to the rapid rise in $\delta B/B$ at storm onset also deviate from the linear regression trend; these data are also from the strong-stretching phase early in the storm. As can be seen by examining the three panels of Figure 26, these data points from the strong-stretching era (from day 1 of the storm and from the ramp up of $\delta B/B$ near storm onset) could be fit separately with a linear regression: a line parallel to the plotted lines would result but with $\delta B/B$ increased by a factor of about 1.4 for all three panels of Figure 26. This deviation from the linear regression trend during the strong-stretching

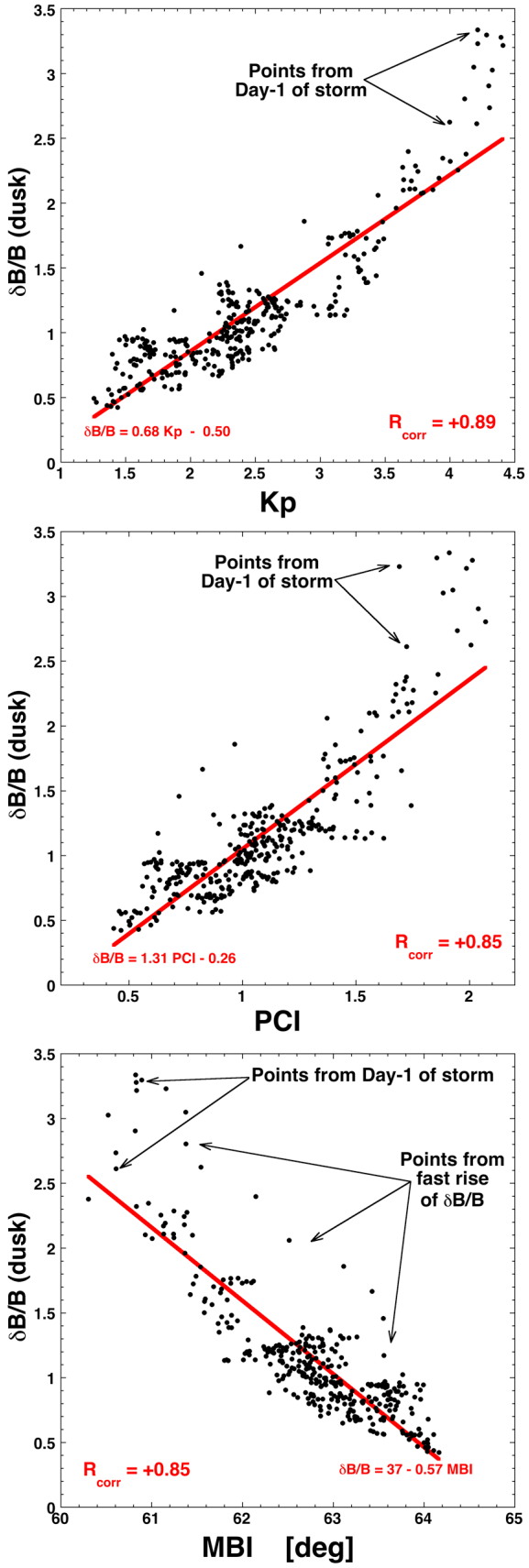

Figure 26. For 63 high-speed stream-driven storms, the 12 h running average of the superposed average of the normalized amplitude $\delta B/B$ of the 1 min magnetic vector changes in the dusk sector of geosynchronous orbit are plotted as functions of (top) the superposed average of the Kp index, (middle) the polar cap index, and (bottom) the midnight boundary index. The data are from 7 days prior to storm onset to 7 days after onset.

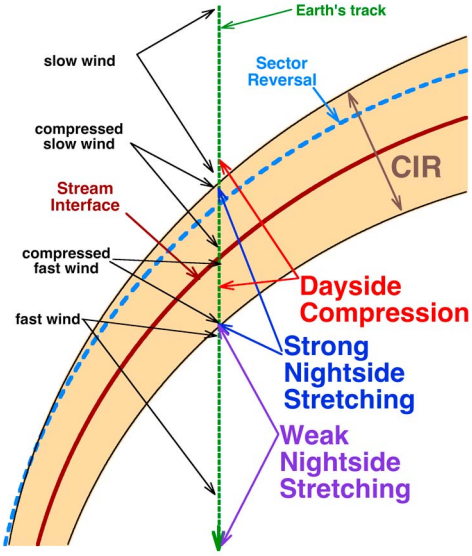

Figure 27. A sketch of a CIR (tan shading) and the Earth's temporal track (green dashed arrow) through the CIR. The temporal region on the time track where the dayside compression of the magnetosphere occurs is labeled in red, the temporal region on the time track where the strong nightside stretching occurs is labeled in blue, and the temporal region on the time track where the weak nightside stretching occurs is labeled in purple.

phase is most prominent in the dusk and midnight sectors. At this time, the reason for the stronger $\delta B/B$ amplitude relative to the strength of the geomagnetic indices during the strong-stretching phase of the magnetosphere is not known.

9. Discussion: The Magnetospheric Magnetic Field and the Solar Wind

[77] To put the dayside compression and nightside stretching of the geosynchronous magnetic field into perspective during the sequence of events of high-speed stream-driven magnetic storms, the timing of the geosynchronous magnetic perturbations relative to the sequence of events in the solar wind associated with the passage of a CIR is explored in section 9.1. A related matter, the ease or difficulty of describing the geosynchronous magnetic field perturbations in terms of upstream solar wind parameters, is discussed in section 9.2.

9.1. Timing of the Magnetic Field Perturbations Relative to Solar Wind Timing and Other Magnetospheric Phenomena

[78] In Figure 27, a corotating interaction region is sketched in the ecliptic plane at Earth's orbit [after *Borovsky and Steinberg*, 2006]. In Figure 27, the Earth's temporal track through the CIR is denoted as the green dashed arrow, and the temporal regions wherein the dayside magnetosphere is compressed (red), wherein the nightside magnetosphere undergoes strong stretching (blue), and wherein the nightside magnetosphere undergoes weak stretching (purple) are indicated along the Earth's track. Also indicated in the sketch are the stream interface separating the compressed slow wind from the compressed fast wind within the CIR, the IMF sector reversal within the compressed slow wind, and the outer boundaries of the CIR (taken to be the width of the compression region of the solar wind magnetic field or the width of the region over which the solar wind speed changes [*Borovsky and Denton*, 2009a]). The Earth begins its track (top to bottom) in slow solar wind (cool ions, lumpy density, low ion specific entropy), then encounters the onset of the CIR and enters into the compressed slow wind, then it crosses the sector reversal within the compressed slow wind, then encounters the stream interface and enters into compressed fast wind, and finally crosses out of the CIR into unperturbed fast wind (hot ions, low density, high ion specific entropy).

9.1.1. Dayside Compression

[79] Examining the dayside magnetosphere magnetic field compression $|B|$ in Figure 8 (bottom, black curve) and comparing that temporal pattern with the patterns of the solar wind parameters in Figure 1, several details about the timing of the dayside compression can be obtained. The dayside magnetic field compression is roughly coincident with the solar wind density increase prior to and within the CIR. (This is exemplified more clearly in Figure 8, where the temporal profile of the dayside field compression is compared with the temporal profile of the solar wind ram pressure, which is enhanced owing to an enhanced solar wind density.) The dayside compression perturbation begins when the Earth is in the slow solar wind before the onset of the CIR and the compression perturbation $|B|$ is about at its maximum when the Earth encounters the IMF sector reversal in the compressed slow wind. When the Earth encounters the CIR stream interface, the dayside compression $|B|$ is declining. The dayside compression ends during the passage of the compressed fast wind before the CIR is exited. These timing observations are entered into Table 1. As stated, the peak in the magnetospheric field compression occurs near the time of passage of the IMF sector reversal; this peak could be caused by noncompressive density enhancements in the slow solar wind that are often associated with sector reversals [cf. *Gosling et al.*, 1981; *Borrini et al.*, 1981; *Crooker et al.*, 1996, 2004a, 2004b; *Blanco et al.*, 2006].

9.1.2. Strong Nightside Stretching

[80] Examining the stretching θ of the nightside magnetic field in Figure 14 (red curve) and comparing that temporal pattern with the patterns of the solar wind parameters in Figure 1, several details about the timing of the nightside stretching can be obtained. The strong-stretching perturbation θ commences at about the time the Earth passes the IMF sector reversal and the stretching θ peaks as the IMF B_z (GSM) is weakening. The strong-stretching perturbation ends at about the time the Earth exits the CIR into the unperturbed fast wind. These timing observations are entered into Table 1. The entire strong-stretching perturbation of the nightside magnetosphere is approximately coincident with the solar wind magnetic field compression, which denotes the major portion of the entire CIR. The strong nightside-stretching perturbation commences after the dayside compression perturbation commences, and the strong nightside-stretching perturbation terminates after the dayside compression per-

Table 1. Typical Chronology of a Recurring High-Speed Stream Cycle and the Resulting Geomagnetic Activity, Behavior of the Earth's Plasma Sheet, Behavior of the Drainage Plumes, Phase of the Relativistic Electron Dropout, and Morphology of the Magnetic Field at Geosynchronous Orbit

Solar Wind at Earth	Stage of Geomagnetic Activity	Solar Wind Density	Plasma Sheet	Plasmasphere	Electron Radiation Belt	Magnetic Field
Slow wind	Calm occurs ~70% of time	Density modest	Ordinary density; ordinary temperature	Plasmasphere growing	Relativistic electron flux slow decay	Compression starts; weak stretching
CIR starts	Calm ends	Density lumpy	Ordinary density; ordinary temperature	Plasmasphere	Relativistic electron flux slow decay	Increasing compression; weak stretching
Compressed slow wind (westward flow)	Mild geomagnetic activity	Density rising	Ordinary density; ordinary temperature	Plasmasphere	Relativistic electron flux slow decay	Increasing compression; weak stretching
Sector reversal in compressed slow wind	Geomagnetic activity rises	Density high	Superdense starts; extra hot starts	Plasmasphere	Relativistic electron flux slow decay	Increasing compression; increasing stretching
Compressed slow wind with southward IMF	Storm onset	Density high	Superdense; extra hot	Plume starts; plasma becomes lumpy	Onset of flux dropout	Increasing compression; strong stretching
Stream interface (flow reversal)	Storm levels	Density declining	Superdense reaches dayside	Plume strong, lumpy	Dropout ongoing	Compression peaks; increasing stretching
Compressed fast wind (eastward flow)	Storm levels	Density modest	Superdense; extra hot	Plume weakening, lumpy	Recovery of flux dropout commences	Decreasing compression; stretching peaks and declines
CIR ends	Storm levels	Density low	Superdense ceases; extra hot continues	Plume weak and lumpy	Recovery progressing	No compression; modest stretching
Fast wind	Activity slowly declines	Density low	Ordinary density; extra hot	Plume weak and lumpy	Recovery complete	No compression; modest stretching slowly declines

turbation terminates. In section 6, it was seen that the timing of the strong nightside stretching perturbation was associated with the timing of the superdense plasma sheet. It is reasonable to believe (e.g., Figures 18 and 19) that the strong nightside stretching early in the storm is associated with diamagnetism from the high plasma pressure in the nightside magnetosphere [cf. *Borovsky et al.*, 1998a]. The higher-than-normal plasma pressure comes with the superdense plasma sheet, which has its origin in the compressed slow wind of the CIR with a few hour time lag going from the solar wind to the nightside of geosynchronous orbit [*Denton and Borovsky*, 2009].

9.1.3. Weak Nightside Stretching

[81] Examining the stretching θ of the nightside magnetic field in Figure 14 (red curve) and comparing that temporal pattern with the patterns of the solar wind parameters in Figure 1, it is seen that there is a persistent (days) modest stretching to the magnetic field on the nightside when the Earth is in the fast wind after the passage of the CIR. This is entered into Table 1. It can be speculated that the long-duration weak stretching is caused by long-duration activity driven by the fast solar wind, with no particular density feature of the solar wind to blame.

9.1.4. Dropout and Recovery of the Radiation Belt

[82] In section 7, it was seen that the strong nightside stretching at geosynchronous orbit was temporally associated with the dropout and recovery of the local time-averaged relativistic electron flux at geosynchronous orbit (see Figure 21). When the number density of the electron radiation belt was examined, it was found that there was no clear temporal association between the dropout and recovery of the density and the strong nightside stretching. The relativistic electron flux dropout and recovery also showed temporal association with the increase and decrease of the magnetopause magnetic field (as calculated from the increase and decrease of the solar wind ram pressure), but again, the number density dropout and recovery lacked an unambiguous temporal association with the magnetopause field strength.

9.1.5. Heating of the Radiation Belt

[83] In section 7, it was noted that the flux of relativistic electrons in the outer electron radiation belt grows steadily in the days after storm onset (see Figure 21). This increase in flux is associated with a heating of the outer electron radiation belt during high-speed stream-driven storms. After recovery of the radiation belt, this heating occurs during the weak-stretching phase of the nightside magnetic field. Determining the physical mechanisms that produce these increasing fluxes of relativistic electrons during high-speed stream-driven storms is among the most important problems being studied in radiation belt physics [cf. *Friedel et al.*, 2002; *Hudson et al.*, 2008]. A causal connection between the weak stretching and the heating of the outer electron radiation belt cannot be made at this time.

[84] These observations about the timing of the magnetospheric magnetic field perturbations during high-speed stream-driven storms are collected into the last column of Table 1. The other columns of Table 1 are assembled from observations gleaned in previous superposed-epoch investigations of high-speed stream-driven storms [cf. *Denton et al.*, 2009c; *Denton and Borovsky*, 2009; *Borovsky and Denton*, 2009c].

9.2. Parameterizing the Magnetospheric Magnetic Field in Terms of Solar Wind Parameters

[85] In Figures 8 and 9, it was seen that the dayside compression perturbation $|B|$ at geosynchronous orbit seemed to be closely related to the ram pressure of the solar wind at Earth. Modeling the dayside compression in terms of upstream solar wind parameters is entirely plausible. In fact, the empirical relation between the dayside geosynchronous orbit magnetic field strength $|B|$ (in nT) and the solar wind ram pressure P_{ram} (in nPa) obtained here was $|B| = B = 106 + 6.3\ P_{ram}$ (expression (2)).

[86] Parameterizing the nightside stretching of the magnetic field in terms of upstream solar wind parameters will not be so straightforward. In Figure 28 (bottom), the superposed average of the stretching angle θ in the midnight sector of geosynchronous orbit is plotted as a function of time, with the zero epoch (black dashed vertical line) taken to be storm onset. The peak of the stretching is marked with a red vertical dashed line and the approximate onset and termination of the strong-stretching phase are marked with two green vertical dashed lines. In Figure 28 (top), the superposed averages of two geomagnetic indices (Kp and Dst) are plotted and in the third through fifth panels of Figure 28 the superposed averages of three upstream-solar wind parameters are plotted (B_z, vB_z, and n). With the green and red vertical lines to guide the eye, it is clearly seen (1) that the timing of the strong-stretching phase of the geosynchronous magnetic field differs from the timing of the plotted geomagnetic indices and solar wind parameters and (2) that without a time lag the temporal profile of the stretching angle θ does not match the temporal profiles of the geomagnetic indices or the solar wind parameters. With a time lag the profile of θ may be matched up with the profile of the solar wind number density n.

[87] The strong nightside-stretching perturbation of the magnetosphere at geosynchronous orbit was found to be coincident with the temporal increase of the particle pressure of the ion plasma sheet on the nightside at geosynchronous orbit (cf. Figures 18 and 19). That particle pressure is owed to elevated plasma sheet number densities (the superdense plasma sheet) and to elevated plasma sheet temperatures (the extra hot plasma sheet). The elevated plasma sheet number density is owed to the increased solar wind density of the compressed slow wind of the CIR, with a time lag of a few hours for the dense solar wind plasma to enter into the magnetosphere and to reach geosynchronous orbit [*Borovsky et al.*, 1998b; *Denton and Borovsky*, 2009]. The elevated plasma sheet temperature is owed to the increased velocity of the solar wind as the CIR passes the Earth; the onset of the extra hot phase of the plasma sheet lags the onset of the superdense phase by a few hours [cf. *Denton and Borovsky*, 2009, Figure 8]. The enhanced plasma sheet pressure being a

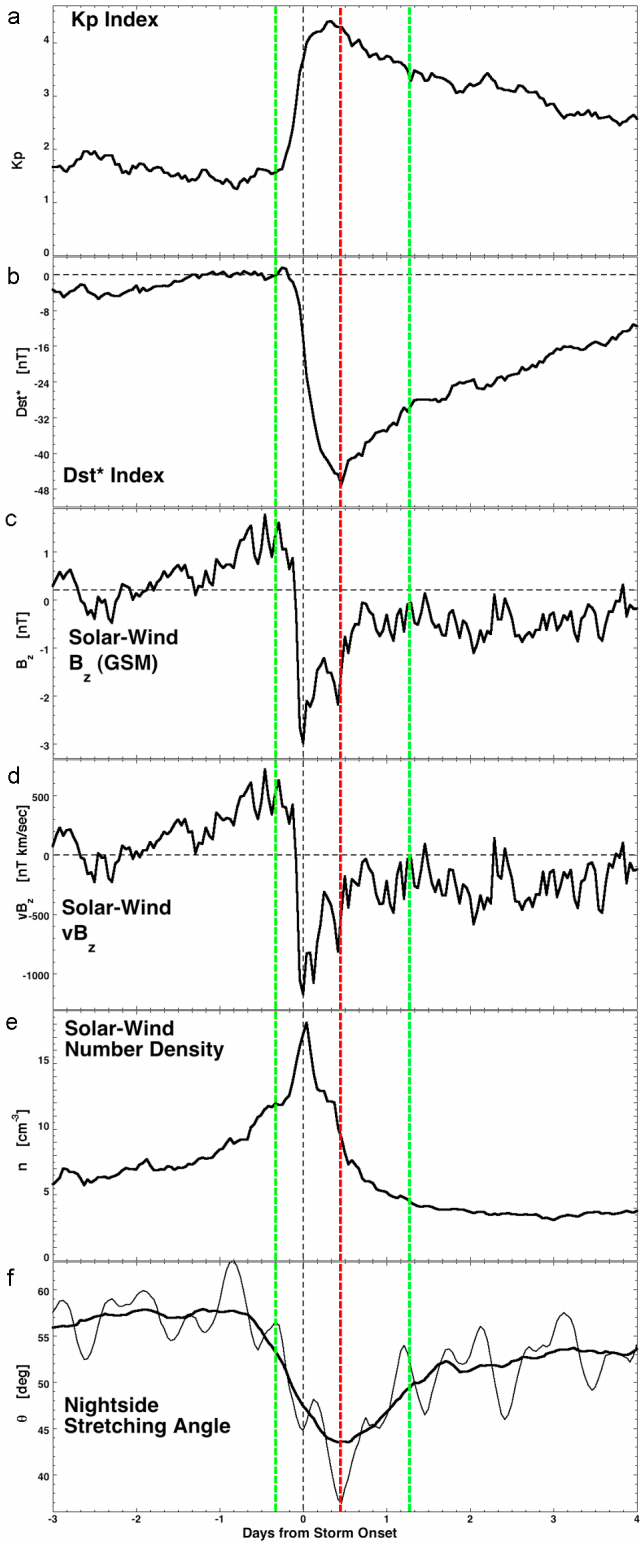

Figure 28. For the 63 high-speed stream-driven storms, the superposed average of the magnetic field stretching angle θ in the midnight sector of geosynchronous orbit as measured by five GOES satellites is plotted as a function of time from storm onset in the bottom. (The thin curve is a 6 h running average and the thick curve is a 24 h running average.) Also plotted are the superposed averages of (top) the Kp index, (second panel) the Dst index, (third panel) B_z (GSM) of the solar wind, (fourth panel) vB_z of the solar wind, and (fifth panel) the number density of the solar wind. The black vertical dashed line is storm onset, the red vertical dashed line is the time at which the magnetic field stretching is maximum, and the two green vertical dashed lines denote the beginning and end of the strong-stretching phase.

combination of the enhanced density and the enhanced temperature, the time lags add to produce an enhanced pressure perturbation that lags the solar wind density perturbation by several hours (cf. Figure 18).

[88] With careful work, a parameterization of the magnetic field stretching at various locations in the magnetosphere in terms of the solar wind number density and velocity with appropriate (location-dependent) time lags could be developed.

10. Summary of Findings

[89] In this report superposed-epoch analysis was used to study changes in the magnetospheric magnetic field at geosynchronous orbit and the relation of those changes to the solar wind, to the plasma sheet, and to the outer electron radiation belt. Sixty-three high-speed stream-driven storms from 1995–2005 were utilized in the analysis of geosynchronous orbit measurements from GOES, MPA, and SOPA, solar wind measurements from OMNI2, and the geomagnetic indices Kp, MBI, and PCI. The findings of the study are listed as follows.

[90] 1. Compression of the magnetic field strength at geosynchronous orbit is mainly on the dayside during high-speed stream-driven storms.

[91] 2. The compression of the dayside magnetic field is simultaneous with an increase in solar wind ram pressure associated with enhanced solar wind density before and within the CIR.

[92] 3. For high-speed stream-driven storms, the compression of the dayside magnetosphere commences before storm onset.

[93] 4. Depending on how the data from the 63 high-speed stream-driven storms is analyzed to remove the effect of solar wind ram pressure on the Dst index, four different expressions for Dst* are obtained and a wide range in Dst* time profiles result. The recommended formula for high-speed stream-driven storms is $Dst^* = Dst - 20.7P_{ram}^{1/2} + 27.7$.

[94] 5. The stretching of the magnetic field at geosynchronous orbit during high-speed stream-driven storms in concentrated on the nightside.

[95] 6. The stretching of the magnetic field on the nightside during high-speed stream-driven storms has two phases: a strong-stretching phase during the first day of the storm and a modest-stretching phase that lasts for several days. The dawn and dusk sectors only exhibit the long-lived modest-stretching phase.

[96] 7. The strong-stretching phase is associated with a perturbation in the Dst* index that contributes to 15%–37% of the total value of Dst* during the high-speed stream-driven storms, depending on the coefficients used for Dst*. The favored value is 20%–25%. This is interpreted as the tail current fractional contribution to Dst*.

[97] 8. The strong stretching phase is temporally associated with the occurrence of the superdense plasma sheet on the nightside during high-speed stream-driven storms.

[98] 9. The strong stretching appears to be caused by anomalously high ion pressure in the magnetosphere.

[99] 10. The temporal profile of global relativistic electron flux dropout and recovery at geosynchronous orbit matches the temporal profile of the nightside strong stretching and relaxation at geosynchronous orbit.

[100] 11. The number density dropout of the outer electron radiation belt occurs early in the strong-stretching phase and the number density recovery of the outer electron radiation belt commences before the stretching has reached its maximum.

[101] 12. Comparison between geosynchronous magnetic field strengths and estimated magnetopause field strengths during the dayside compression phase indicates that magnetopause shadowing should be important for dropping out the nightside outer electron radiation belt during high-speed stream-driven storms.

[102] 13. The amplitude δB of temporal (1 min) changes in the magnetic field vector at geosynchronous orbit increases substantially at storm onset and then decays slowly in the days of the storm.

[103] 14. The normalized amplitude $\delta B/B$ of temporal changes in the magnetic field vector at geosynchronous orbit is linearly proportional to several geomagnetic indices (Kp, PCI, and MBI).

[104] 15. Whereas parameterization of the dayside compression of the geosynchronous magnetic field is simple in terms of upstream solar wind parameters (i.e., ram pressure), parameterization of the nightside magnetic field stretching in terms of the upstream solar wind (i.e., number density and speed) will require time lags to be implemented.

[105] **Acknowledgments.** The authors wish to thank Howard Singer for help with the GOES data, Tom Cayton for relativistic Maxwellian fits to the SOPA data, and Joachim Birn, Steve Morley, and Howard Singer for useful conversations. J.E.B. wishes to thank the Department of Communication Systems at Lancaster University for their hospitality. Research at Los Alamos was supported by the NASA Targeted Research and Technology Program and by the Los Alamos National Laboratory LDRD Program. Research at Lancaster was supported by the STFC-grant ST/G002401/1.

[106] Philippa Browning thanks Barbara Emery and another reviewer for their assistance in evaluating this paper.

References

Abdu, M. A., R. J. de Souza, J. H. A. Sobral, and I. S. Batista (2006), Magnetic storm associated disturbance dynamo effects in the low and equatorial latitude ionosphere, in *Recurrent Magnetic Storms*, edited by B. Tsurutani et al., p. 283, AGU, Washington, D. C.

Alexeev, I. I., and Y. I. Feldstein (2001), Modeling of geomagnetic field during magnetic storms and comparison with observations, *J. Atmos. Sol. Terr. Phys.*, 63, 431–440.

Alexeev, I. I., E. S. Belenkaya, V. V. Kalegaev, Y. I. Feldstein, and A. Grafe (1996), Magnetic storms and magnetotail currents, *J. Geophys. Res.*, 101(A4), 7737–7747.

Anderson, B. J., M. J. Engebretson, S. P. Rounds, L. J. Zanetti, and T. A. Potemra (1990), A statistical study of Pc 3–5 pulsations observed by the AMPTE/CCE magnetic fields experiment 1. Occurrence distributions, *J. Geophys. Res.*, 95(A7), 10,495–10,523.

Baker, D. N., R. L. McPherron, T. E. Cayton, and R. W. Klebesadel (1990), Linear prediction filter analysis of relativistic electron properties at 6.6 R_E, *J. Geophys. Res.*, 95(A9), 15,133–15,140.

Bame, S. J., D. J. McComas, M. F. Thomsen, B. L. Barraclough, R. C. Elphic, J. P. Glore, J. T. Gosling, J. C. Chavez, E. P. Evans, and F. J. Wymer (1993), Magnetospheric plasma analyzer for spacecraft with constrained resources, *Rev. Sci. Instrum.*, 64, 1026–1033.

Bartels, J., and J. Veldkamp (1949), International data on magnetic disturbances, First Quarter, 1949, *J. Geophys. Res.*, 54(3), 295–299.

Belian, R. D., G. R. Gisler, T. Cayton, and R. Christensen (1992), High-Z energetic particles at geosynchronous orbit during the great solar proton event series of October 1989, *J. Geophys. Res.*, 97(A11), 16,897–16,906.

Belian, R. D., T. E. Cayton, R. A. Christensen, J. C. Ingraham, M. M. Meier, G. D. Reeves, and A. J. Lazarus (1996), Relativisitic electrons in the outer-zone: An 11 year cycle; their relation to the solar wind, in *Workshop on the Earth's Trapped Particle Environment*, edited by G. D. Reeves, p. 13, American Institute of Physics, Woodbury, New York.

Blake, J. B., R. S. Selesnick, D. N. Baker, and S. Danekal (2001), Studies of relativistic electron injection events in 1997 and 1998, *J. Geophys. Res.*, 106(A9), 19,157–19,168.

Blanco, J. J., J. Rodriquez-Pacheco, M. A. Hidalgo, and J. Sequeiros (2006), Analysis of the heliospheric current sheet fine structure: Single or multiple currents sheets, *J. Atmos. Sol. Terr. Phys.*, 68, 2173–2181.

Borodkova, N. L., J.-B. Liu, Z.-H. Huang, G. N. Zastenker, C. Wang, and P. E. Eiges (2006), Effect of change in large and fast solar wind dynamic pressure on geosynchronous magnetic field, *Chin. Phys.*, 15, 2458–2464.

Borodkova, N. L., J. B. Liu, Z. H. Huang, and G. N. Zastenker (2008), Geosynchronous magnetic field response to the large and fast solar wind dynamic pressure changes, *Adv. Space Res.*, 41, 1220–1225.

Borovsky, J. E. (2008), The flux tube texture of the solar wind: Strands of the magnetic carpet at 1 AU, *J. Geophys. Res.*, 113(A8), A08110, doi:10.1029/2007JA012684.

Borovsky, J. E. (2010), On the variations of the solar wind magnetic field about the Parker-spiral direction, *J. Geophys. Res.*, doi:10.1029/2009JA015040, in press.

Borovsky, J. E., and M. H. Denton (2006), The differences between CME-driven storms and CIR-driven storms, *J. Geophys. Res.*, 111(A7), A07S08, doi:10.1029/2005JA011447.

Borovsky, J. E., and M. H. Denton (2008), A statistical look at plasmaspheric drainage plumes, *J. Geophys. Res.*, 113(A9), A09221, doi:10.1029/2007JA012994.

Borovsky, J. E., and M. H. Denton (2009a), Solar-wind turbulence and shear: A superposed-epoch analysis of corotating interaction regions at 1 AU, *J. Geophys. Res.*, doi:10.1029/2009JA014966, in press.

Borovsky, J. E., and M. H. Denton (2009b), Electron loss rates from the outer electron radiation belt caused by the filling of the outer plasmasphere: The calm before the storm, *J. Geophys. Res.*, 114(A11), A11203, doi:10.1029/2009JA014063.

Borovsky, J. E., and M. H. Denton (2009c), Relativistic electron dropouts and recovery: A superposed-epoch study of the magnetosphere and the solar wind, *J. Geophys. Res.*, 114(A2), A02201, doi:10.1029/2008JA013128.

Borovsky, J. E., and J. T. Steinberg (2006), The "calm before the storm" in CIR/magnetosphere interactions: Occurrence statistics, solar wind statistics, and magnetospheric preconditioning, *J. Geophys. Res.*, 111(A7), A07S10, doi:10.1029/2005JA011397.

Borovsky, J. E., M. F. Thomsen, D. J. McComas, T. E. Cayton, and D. J. Knipp (1998a), Magnetospheric dynamics and mass flow during the November 1993 storm, *J. Geophys. Res.*, 103(A11), 26,373–26,394.

Borovsky, J. E., M. F. Thomsen, and R. C. Elphic (1998b), The driving of the plasma sheet by the solar wind, *J. Geophys. Res.*, 103(A8), 17,617–17,639.

Borovsky, J. E., M. F. Thomsen, R. C. Elphic, T. E. Cayton, and D. J. McComas (1998c), The transport of plasma sheet material from the distant tail to geosynchronous orbit, *J. Geophys. Res.*, 103(A9), 20,297–20,331.

Borovsky, J. E., B. Lavraud, and M. M. Kuznetsova (2009). Polar cap potential saturation, dayside reconnection, and changes to the magnetosphere, *J. Geophys. Res.*, 114(A3), A03224, doi:10.1029/2009JA014058.

Borrini, G., J. T. Gosling, S. J. Bame, W. C. Feldman, and J. M. Wilcox (1981), Solar wind helium and hydrogen structure near the heliospheric current sheet: A signal of coronal streamers at 1 AU, *J. Geophys. Res.*, 86(A6), 4565–4573.

Bortnik, J., R. M. Thorne, T. P. O'Brien, J. C. Green, R. J. Strangeway, Y. Y. Shprits, and D. N. Baker (2006), Observation of two distinct, rapid loss mechanisms during the 20 November 2003 radiation belt dropout event, *J. Geophys. Res.*, 111(A12), A12216, doi:10.1029/2006JA011802.

Brautigam, D. H., and J. M. Albert (2000), Radial diffusion analysis of outer radiation belt electrons during the October 9, 1990 magnetic storm, *J. Geophys. Res.*, 105(A1), 291–309.

Burlaga, L. F. (1974), Interplanetary stream interfaces, *J. Geophys. Res.*, 79(25), 3717–3725.

Burlaga, L. F., and R. P. Lepping (1977), The causes of recurrent geomagnetic storms, *Planet. Space Sci.*, 25, 1151–1160.

Burlaga, L. F., W. H. Mish, and Y. C. Whang (1990), Coalescence of recurrent streams of different sizes and amplitudes, *J. Geophys. Res.*, 95(A4), 4247–4255.

Burton, M. E., M. Neugebauer, N. U. Crooker, R. von Steiger, and E. J. Smith (1999), Identification of trailing edge solar wind stream interfaces: A comparison of Ulysses plasma and compositional measurements, *J. Geophys. Res.*, 104(A5), 9925–9932.

Burton, P. K., R. L. McPherron, and C. T. Russell (1975), An empirical relationship between interplanetary conditions and Dst, *J. Geophys. Res.*, 80(31), 4204–4214.

Cayton, T. E., and R. D. Belian (2007), Numerical modeling of the synchronous orbit particle analyzer (SOPA, Version 2) that flew on S/C 1990-095, *LA Rep. LA-14335*, Los Alamos Natl. Lab., Los Alamos, N. M.

Cayton, T. E., R. D. Belian, S. P. Gary, T. A. Fritz, and D. N. Baker (1989), Energetic electron components at geosynchronous orbit, *Geophys. Res. Lett.*, 16(2), 147–150.

Chang, L. C., J. P. Thayer, J. Lei, and S. E. Palo (2009), Isolation of the global MLT thermal response to recurrent geomagnetic activity, *Geophys. Res. Lett.*, 36(15), L15813, doi:10.1029/2009GL039305.

Crooker, N. U., and E. W. Cliver (1994), Postmodern view of M regions, *J. Geophys. Res.*, 99(A12), 23,383–23,390.

Crooker, N. U., M. E. Burton, G. L. Siscoe, S. W. Kahler, J. T. Gosling, and E. J. Smith (1996), Solar wind streamer belt structure, *J. Geophys. Res.*, 101(A11), 24,331–24,341.

Crooker, N. U., C.-L. Huang, S. M. Lamassa, D. E. Larson, S. W. Kahler, and H. E. Spence (2004a), Heliospheric plasma sheets, *J. Geophys. Res.*, 109(A3), A03107, doi:10.1029/2003JA010170.

Crooker, N. U., S. W. Kahler, D. E. Larson, and R. P. Lin (2004b), Large-scale magnetic field inversions at sector boundaries, *J. Geophys. Res.*, 109(A3), A03108, doi:10.1029/2003JA010278.

Denton, M. H., and J. E. Borovsky (2008), Superposed-epoch analysis of high-speed-stream effects at geosynchronous orbit: Hot plasma, cold plasma, and the solar wind, *J. Geophys. Res.*, 113(A7), A07216, doi:10.1029/2007JA012998.

Denton, M. H., and J. E. Borovsky (2009), The superdense plasma sheet in the magnetosphere during high-speed-steam-driven storms: Plasma transport time scales, *J. Atmos. Sol. Terr. Phys.*, 71, 1045–1058.

Denton, M. H., J. E. Borovsky, R. M. Skoug, M. F. Thomsen, B. Lavraud, M. G. Henderson, R. L. McPherron, J. C. Zhang, and M. W. Liemohn (2006), Geomagnetic storms driven by ICME- and CIR-dominated solar wind, *J. Geophys. Res.*, 111(A7), A07S07, doi:10.1029/2005JA011436.

Denton, M. H., J. E. Borovsky, R. B. Horne, R. L. McPherron, S. K. Morley, and B. T. Tsurutani (2008), High-speed solar wind streams: A call for key research, *Eos Trans. AGU*, *89*(7), doi:10.1029/2008EO070002.

Denton, M. H., T. Ulich, and E. Turünen (2009a), Modification of midlatitude ionospheric parameters in the F2 layer by persistent high-speed solar wind streams, *Space Weather*, 7, S04006, doi:10.1029/2008SW000443.

Denton, M. H., J. E. Borovsky, R. B. Horne, R. L. McPherron, S. K. Morley, and B. T. Tsurutani (2009b), Introduction to special issue on high speed solar wind streams and geospace interactions (HSS-GI), *J. Atmos. Sol. Terr. Phys.*, 71, 1011–1013.

Denton, M. H., J. E. Borovsky, and T. E. Cayton (2009c), A density-temperature description of the outer electron radiation belt during geomagnetic storms, *J. Geophys. Res.*, 115(A1), A01208, doi:10.1029/2009JA014183.

Desorgher, L., E. Fluckiger, P. Buhler, and A. Zehnder (2000), Modelling of the outer electron belt flux dropout and losses during magnetic storm main phase, *Adv. Space Res.*, 26, 167–171.

Dessler, A. J., and E. N. Parker (1959), Hydromagnetic theory of geomagnetic storms, *J. Geophys. Res.*, 64(12), 2239–2252.

Dessler, A. J., and R. Karplus (1961), Some effects of diamagnetic ring currents on Van Allen radiation, *J. Geophys. Res.*, 66(8), 2289–2295.

Dunham, W. D., S. A. MacIntyre, and C. R. Upton (1996), Design and performance of the GOES-8 high resolution magnetometer, *SPIE Proc.*, 2812, 365–374.

Elkington, S. R., M. K. Hudson, and A. A. Chan (2003), Resonant acceleration and diffusion of outer zone electrons in an asymmetric geomagnetic field, *J. Geophys. Res.*, 108(A3), 1116, doi:10.1029/2001JA009202.

Elphic, R. C., M. F. Thomsen, J. E. Borovsky, and D. J. McComas (1999), Inner edge of the electron plasma sheet: Empiracal models of boundary location, *J. Geophys. Res.*, 104(A10), 22,679–22,693.

Fairfield, D. H. (1964), Trapped particles in a distorted dipole field, *J. Geophys. Res.*, 69(19), 3919–3926.

Fälthammar, C.-G. (1965), Effects of time-dependent electric fields on geomagnetically trapped radiation, *J. Geophys. Res.*, 70(11), 2503–2516.

Feldstein, Y. I., V. Y. Pisarsky, R. M. Rudneva, and A. Grafe (1984), Ring current simulation in connection with interplanetary space conditions, *Planet. Space Sci.*, 32, 975–984.

Forsyth, R. J., and E. Marsch (1999), Solar origin and interplanetary evolution of stream interfaces, *Space Sci. Rev.*, 89, 7–20.

Freeman, J. W. (1964), The morphology of the electron distribution in the outer radiation zone and near the magnetospheric boundary as observed by Explorer 12, *J. Geophys. Res.*, 69(9), 1691–1723.

Friedel, R. H. W., G. D. Reeves, and T. Obara (2002), Relativistic electron dynamics in the inner magnetophere – A review, *J. Atmos. Sol. Terr. Phys.*, 64, 265.

Fritz, T. A., M. Alothman, J. Bhattacharjya, D. L. Matthews, and J. Chen (2003), Butterfly pitch angle distributions observed by ISEE-1, *Planet. Space Sci.*, 51(3), 205–219.

Gonzalez, W. D., B. T. Tsurutani, and A. L. Clua de Gonzalez (1999), Interplanetary origin of geomagnetic storms, *Space Sci. Rev.*, 88, 529–562.

Gosling, J. T., J. R. Asbridge, S. J. Bame, and W. C. Feldman (1978), Solar wind stream interfaces, *J. Geophys. Res.*, 83(A4), 1401–1412.

Gosling, J. T., G. Borrini, J. R. Asbridge, S. J. Bame, W. C. Feldman, and R. T. Hansen (1981), Coronal streamers in the solar wind at 1 AU, *J. Geophys. Res.*, 86(A7), 5438–5448.

Gosling, J. T., D. J. McComas, J. L. Phillips, and S. J. Bame (1991), Geomagnetic activity associated with Earth passage of interplanetary shock disturbances and coronal mass ejections, *J. Geophys. Res.*, 96(A5), 7831–7839.

Green, J. C., T. G. Onsager, T. P. O'Brien, and D. N. Baker (2004), Testing loss mechanisms capable of rapidly depleting relativistic electron flux in the Earth's outer radiation belt, *J. Geophys. Res.*, 109(A12), A12211, doi:10.1029/2004JA010579.

Gussenhoven, M. S., D. A. Hardy, and N. Heinemann (1983), Systematics of the equatorward diffuse auroral boundary, *J. Geophys. Res.*, 88(A7), 5692–5708.

Heppner, J. P., N. F. Ness, C. S. Scearce, and T. L. Skillman (1963), Explorer 10 magnetic field measurements, *J. Geophys. Res.*, 68(1), 1–46.

Hones, E. W. (1963), Motions of charged particles trapped in the Earth's magnetosphere, *J. Geophys. Res.*, 68(5), 1209–1219.

Horne, R. B., and R. M. Thorne (1998), Potential waves for relativistic electron scattering and stochastic acceleration during magnetic storms, *Geophys. Res. Lett.*, 25(15), 3011–3014, doi:10.1029/98GL01002.

Huang, C.-L., H. E. Spence, J. G. Lyon, F. R. Toffoletto, H. J. Singer, and S. Sazykin (2006), Storm-time configuration of the inner magnetosphere: Lyon-Fedder-Mobarry MHD code, Tsyganenko model, and GOES observations, *J. Geophys. Res.*, 111(A11), A11S16, doi:10.1029/2006JA011626.

Huang, C.-L., H. E. Spence, H. J. Singer, and N. A. Tsyganenko (2008), A quantitative assessment of empirical magnetic field models at geosynchronous orbit during magnetic storms, *J. Geophys. Res.*, 113(A4), A04208, doi:10.1029/2007JA012623.

Hudson, M. K., B. T. Kress, H. R. Mueller, J. A. Zastrow, and J. B. Blake (2008), Relationship of the Van Allen radiation belts to solar wind drivers, *J. Atmos. Sol. Terr. Phys.*, 70, 708–729.

Ilie, R., M. W. Liemohn, M. F. Thomsen, J. E. Borovsky, and J. Zhang (2008), Influence of epoch time selection on the results of superposed-epoch analysis using ACE and MPA data, *J. Geophys. Res.*, 114(A3), A00A14, doi:10.1029/2008JA013241.

Johnson, J. R., and S. Wing (2009), Northward interplanetary magnetic field plasma sheet entropies, *J. Geophys. Res.*, 114(A9), A00D08, doi:10.1029/2008JA014017.

Jordanova, V. K., J. Albert, and Y. Miyoshi (2008), Relativistic electron precipitation by EMIC waves from self-consistent global simulations, *J. Geophys. Res.*, 114(A3), A00A10, doi:10.1029/2008JA013239.

Kalegaev, V. V., and E. V. Makarenkov (2008), Relative importance of ring and tail currents to Dst under extremely disturbed conditions, *J. Atmos. Sol. Terr. Phys.*, 70, 519–525.

Kalegaev, V. V., N. Y. Ganushkina, T. I. Pulkkinen, M. V. Kubyshkina, H. J. Singer, and C. T. Russell (2005), Relation between the ring current and the tail current during magnetic storms, *Ann. Geophys.*, 23, 523–533.

Kavanagh, A. J., and M. H. Denton (2007), High-speed solar wind streams and geospace interactions, *Aston. Geophys.*, 48, 6.24–6.26.

Kim, H.-J., and A. A. Chan (1997), Fully adiabatic changes in storm time relativistic electron fluxes, *J. Geophys. Res.*, 102(A10), 22,107–22,116.

Kim, K. C., D.-Y. Lee, H.-J. Kim, L. R. Lyons, E. S. Lee, M. K. Ozturk, and C. R. Choi (2008), Numerical calculations of relativistic electron drift loss effect, *J. Geophys. Res.*, 113(A9), A09212, doi:10.1029/2007JA013011.

Knipp, D. J., et al. (1998), Overview of the early November 1993 geomagnetic storm, *J. Geophys. Res.*, 103(A11), 26,197–26,220.

Lavraud, B., and J. E. Borovsky (2008), The altered solar wind-magnetosphere interaction at low Mach numbers: Coronal mass ejections, *J. Geophys. Res.*, 114(A9), A00B08, doi:10.1029/2008JA013192.

Lazarus, A., J. Dasper, A. Szabo, and K. Ogilvie (2003), Solar wind streams and their interactions, *AIP Conf. Proc.*, 679, 187.

Li, X., D. N. Baker, M. Temerin, T. E. Cayton, E. G. D. Reeves, R. A. Christensen, J. B. Blake, M. D. Looper, R. Nakamura, and S. G. Kanekal (1997), Multisatellite observations of the outer zone electron variation during the November 3–4, 1993, magnetic storm, *J. Geophys. Res.*, 102(A7), 14,123.

Liemohn, M. W., J. U. Kozyra, M. F. Thomsen, J. L. Roeder, G. Lu, J. E. Borovsky, and T. E. Cayton (2001), Dominant role of the asymmetric ring current in producing the stormtime Dst*, *J. Geophys. Res.*, 106(A6), 10,883–10,904.

Longden, N., M. H. Denton, and F. Honary (2008), Particle precipitation during ICME-driven and CIR-driven geomagnetic storms, *J. Geophys. Res.*, 113(A6), A06205, doi:10.1029/2007JA012752.

Love, D. L., D. S. Toomb, D. C. Wilkinson, and J. B. Parkinson (2000), Penetrating electron fluctuations associated with GEO spacecraft anomalies, *IEEE Trans. Plasma Sci.*, 28, 2075–2084.

Mathie, R. A., and I. R. Mann (2000), A correlation between extended intervals of ULF wave power and storm time geosynchronous relativistic electron flux enhancements, *Geophys. Res. Lett.*, 27(20), 3261–3264, doi:10.1029/2000GL003822.

McComas, D. J., S. J. Bame, B. L. Barraclough, J. R. Donart, R. C. Elphic, J. T. Gosling, M. B. Moldwin, K. R. Moore, and M. F. Thomsen (1993), Magnetospheric Plasma Analyzer: Initial 3-spacecraft observations from geosynchronous orbit, *J. Geophys. Res.*, 98(A8), 13,453–13,465.

McComas, D. J., R. C. Elphic, M. B. Moldwin, and M. F. Thomsen (1994), Plasma observations of magnetopause crossings at geosynchronous orbit, *J. Geophys. Res.*, 99(A11), 21,249–21,255.

McPherron, R. L., and J. N. Barfield (1980), A seasonal change in the effect of field-aligned currents at synchronous orbit, *J. Geophys. Res.*, 85(A12), 6743–6746.

McPherron, R. L., and J. Weygand (2006), The solar wind and geomagnetic activity as a function of time relative to corotating interaction regions, in *Recurrent Magnetic Storms*, edited by B. Tsurutani et al., p. 125, AGU, Washington, D. C.

McPherron, R. L., C. T. Russell, and P. J. Coleman (1972), Fluctuating magnetic fields in the magnetosphere, *Space Sci. Rev.*, 13, 411–454.

Mead, G. D. (1964), Deformation of the geomagnetic field by the solar wind, *J. Geophys. Res.*, 69(7), 1181–1195.

Meier, M. M., R. R. D. Belian, T. E. Cayton, R. A. Christensen, B. Garcia, K. M. Grace, J. C. Ingraham, J. G. Laros, and G. D. Reeves (1996), The energy spectrometer for particles (ESP): Instrument description and orbital performance, *AIP Conf. Proc.*, 383, 203–210.

Meredith, N. P., R. B. Horne, S. A. Glaurt, R. M. Thorne, D. Summers, J. M. Albert, and R. R. Anderson (2006), Energetic outer zone electron loss timescales during low geomagnetic activity, *J. Geophys. Res.*, 111(A5), A05212, doi:10.1029/2005JA011516.

Miyoshi, Y., and R. Kataoka (2005), Ring current ions and radiation belt electrons during geomagnetic storms driven by coronal mass ejections and corotating interaction regions, *Geophys. Res. Lett.*, 32(21), L21105, doi:10.1029/2005GL024590.

Miyoshi, Y., A. Morioka, T. Obara, H. Misawa, T. Nagai, and Y. Kasahara (2003), Rebuilding process of the outer radiation belt during the 3 November 1993 magnetic storm: NOAA and Exos-D observations, *J. Geophys. Res.*, 108(A1), 1004, doi:10.1029/2001JA007542.

Moldwin, M. B., M. I. Fernandez, H. K. Rassoul, M. F. Thomsen, S. J. Bame, D. J. McComas, and J. F. Fennell (1998), A reexamination of the local time asymmetry of lobe encounters at geosynchronous orbit: CRRES, ATS-5 and LANL observations, *J. Geophys. Res.*, 103(A5), 9207–9216.

Mursula, K., and B. Zieger (1996), The 13.5-day periodicity in the Sun, solar wind, and geomagnetic activity: The last three solar cycles, *J. Geophys. Res.*, 101(A12), 27,077–27,090.

Nagai, T. (1988), "Space weather forecast": Prediction of relativistic electron intensity at synchronous orbit, *Geophys. Res. Lett.*, 15(5), 425–428.

Neugebauer, M., P. C. Liewer, B. E. Goldstein, X. Zhou, and J. T. Steinberg (2004), Solar wind stream interaction regions without sector boundaries, *J. Geophys. Res.*, 109(A10), A10102, doi:10.1029/2004JA010456.

O'Brien, T. P., and R. L. McPherron (2000), An empirical phase space analysis of ring current dynamics: Solar wind control of injection and decay, *J. Geophys. Res.*, 105(A4), 7707–7719.

Ohtani, S., M. Nose, G. Rostoker, H. Singer, A. T. Y. Lui, and M. Kakamura (2001), Storm-substorm relationship: Contribution of the tail current to Dst, *J. Geophys. Res.*, 106(A10), 21,199–21,209.

Ohtani, S., Y. Ebihara, and H. J. Singer (2007), Storm-time magnetic configurations at geosynchronous orbit: Comparison between the main and recovery phases, *J. Geophys. Res.*, 112(A5), A05202, doi:10.1029/2006JA011959.

Ohtani, S., Y. Miyoshi, H. J. Singer, and J. M. Weygand (2009), On the loss of relativistic electrons at geosynchronous altitude: Its dependence on magnetic configurations and external conditions, *J. Geophys. Res.*, 114(A1), A01202, doi:10.1029/2008JA013391.

Olson, P., and H. Amit (2006), Changes in the Earth's dipole, *Nature*, 93, 519–542.

Onsager, T. G., G. Rostoker, H.-J. Kim, G. D. Reeves, T. Obara, H. J. Singer, and C. Smithro (2002), Radiation belt electron flux dropouts: Local time, radial, and particle-energy dependence, *J. Geophys. Res.*, 107(A11), 1382, doi:10.1029/2001JA000187.

Onsager, T. G., J. C. Green, G. D. Reeves, and H. J. Singer (2007), Solar wind and magnetospheric conditions leading to the abrupt loss of outer radiation belt electrons, *J. Geophys. Res.*, 112(A1), A01202, doi:10.1029/2006JA011708.

Orr, D. (1973), Magnetic pulsations within the magnetosphere: A review, *J. Atmos. Terr. Phys.*, 35, 1–50.

Osherovich, V. A., J. Fainberg, R. G. Stone, A. Vinas, R. Fitzenreiter, and C. J. Farrugia (1999), MHD of gas with polytropic index below unity and classification of magnetic clouds, *AIP Conf. Proc.*, 471, 717–720.

Pagel, A. C., N. U. Crooker, T. H. Zurbuchen, and J. T. Gosling (2004), Correlation of solar wind entropy and oxygen ion charge state ratio, *J. Geophys. Res.*, 109(A1), A01113, doi:10.1029/2003JA010010.

Paulikas, G. A., and J. B. Blake (1976), Modulation of trapped energetic electrons at 6.6 Re by the interplanetary magnetic field, *Geophys. Res. Lett.*, 3(5), 277–280, doi:10.1029/GL003i005p00277.

Perry, K. L., M. K. Hudson, and S. R. Elkington (2005), Incorporating spectral characteristics of Pc5 waves into three-dimensional radiation belt modeling and the diffusion of relativistic electrons, *J. Geophys. Res.*, 110(A3), A03215, doi:10.1029/2004JA010760.

Piddington, J. H. (1960), Geomagnetic storm theory, *J. Geophys. Res.*, 65(1), 93–106.

Prölss, G. W. (2006), Selected upper atmospheric storm effects, in *Recurrent Magnetic Storms*, edited by B. Tsurutani et al., p. 305, AGU, Washington, D. C.

Pudovkin, M. I., S. A. Zaitseva, and L. Z. Sizova (1985), Growth rate and decay of magnetospheric ring current, *Planet. Space Sci.*, 33, 1097–1102.

Reeves, G. D. (1998), Relativistic electrons and magnetic storms: 1992–1995, *Geophys. Res. Lett.*, 25(11), 1817–1820, doi:10.1029/98GL01398.

Richardson, I. G. (2006), The formation of CIRs at stream-stream interfaces and resultant geomagnetic activity, in *Recurrent Magnetic Storms*, edited by B. Tsurutani et al., p. 45, AGU, Washington, D. C.

Richter, A. K., and A. H. Luttrell (1986), Superposed epoch analysis of corotating interaction regions at 0.3 and 1.0 AU: A comparative study, *J. Geophys. Res.*, 91(A5), 5873–5878.

Ridley, A. J., and E. A. Kihn (2004), Polar cap index comparisons with AMIE cross-polar cap potential, electric field, and polar cap area, *Geophys. Res. Lett.*, 31(7), L07801, doi:10.1029/2003GL019113.

Roederer, J. G. (1967), On the adiabatic motion of energetic particles in a model magnetosphere, *J. Geophys. Res.*, 72(3), 981–992.

Rostoker, G. (1972), Geomagnetic indices, *Rev. Geophys. Space Phys.*, 10, 935–950.

Rostoker, G., S. Skone, and D. N. Baker (1998), On the origin of relativistic electrons in the magnetosphere associated with some geomagnetic storms, *Geophys. Res. Lett.*, 25(19), 3701–3704, doi:10.1029/98GL02801.

Rufenach, C. L., R. F. Martin, and H. H. Sauer (1989), A study of geosynchronous magnetopause crossings, *J. Geophys. Res.*, 94(A11), 15,125–15,134.

Russell, C. T., and R. L. McPherron (1973), Semiannual variation of geomagnetic activity, *J. Geophys. Res.*, 78(1), 92–108.

Saito, T. (1969), Geomagnetic pulsations, *Space Sci. Rev.*, 10, 319.

Sandanger, M., F. Sørass, K. Aarsnes, K. Oksavik, and D. S. Evans (2007), Loss of relativistic electrons: evidence for pitch angle scattering by electromagnetic ion cyclotron waves excited by unstable ring current protons, *J. Geophys. Res.*, 112(A12), A12213, doi:10.1029/2006JA012138.

Sanny, J., D. Judnick, M. B. Moldwin, D. Berube, and D. G. Sibeck (2007), Global profiles of compressional ultralow frequency wave power at geosynchronous orbit and their response to the solar wind, *J. Geophys. Res.*, 112(A5), A05224, doi:10.1029/2006JA012046.

Schield, M. A. (1969), Pressure balance between solar wind and magnetosphere, *J. Geophys. Res.*, 74(5), 1275–1286.

Shprits, Y. Y., R. M. Thorne, R. Friedel, G. D. Reeves, J. Fennell, D. N. Baker, and S. G. Kanekal (2006), Outward radial diffusion driven by losses at magnetopause, *J. Geophys. Res.*, 111(A11), A11214, doi:10.1029/2006JA011657.

Shprits, Y. Y., S. R. Elkington, N. P. Meredith, and D. A. Subbotin (2008), Review of modeling of losses and sources of relativistic electrons in the outer radiation belt I: Radial transport, *J. Atmos. Sol. Terr. Phys.*, 70, 1679–1693.

Singer, H. J., L. Matheson, R. Grubb, A. Newman, and S. D. Bouwer (1996), Monitoring space weather with the GOES magnetometers, *SPIE Proc.*, 2812, 299–308.

Siscoe, G., and D. Intriligator (1993), Three views of two giant streams: Aligned observations at 1 AU, 4.6 AU, and 5.9 AU, *Geophys. Res. Lett.*, 20(20), 2267–2270, doi:10.1029/93GL02488.

Siscoe, G. L., and K. D. Siebert (2006), Bimodal nature of solar wind-magnetosphere-ionosphere-thermosphere coupling, *J. Atmos. Sol. Terr. Phys.*, 68, 911–920.

Siscoe, G. L., B. Goldstein, and A. J. Lazarus (1969), An east-west asymmetry in the solar wind velocity, *J. Geophys. Res.*, 74(7), 1759–1762.

Siscoe, G., J. Raeder, and A. J. Ridley (2004), Transpolar potential saturation models compared, *J. Geophys. Res.*, 109(A9), A09203, doi:10.1029/2003JA010318.

Skone, S. H., E. F. Donovan, and G. Rostoker (1995), Characterizing the quiet time magnetic field at geostationary orbit, *J. Geophys. Res.*, 100(A12), 23,583–23,596.

Skoug, R. M., et al. (2003), Tail-dominated storm main phase: 31 March 2001, *J. Geophys. Res.*, 108(A6), 1259, doi:10.1029/2002JA009705.

Sojka, J. J., R. L. McPherron, A. P. van Eyken, M. J. Nicholls, C. J. Heinselman, and J. D. Kelley (2009), Observations of ionospheric heating during the passage of solar coronal hole fast streams, *Geophys. Res. Lett.*, 36(19), L19105, doi:10.1029/2009GL039064.

Spreiter, J. R., A. L. Summers, and A. Y. Alksne (1966), Hydromagnetic flow around the magnetosphere, *Planet. Space Sci.*, 14, 223–250.

Su, S.-Y., and A. Konradi (1975), Magnetic field depression at the Earth's surface calculated from the relationship between the size of the magnetosphere and the Dst values, *J. Geophys. Res.*, 80(1), 195–199.

Summers, D., and R. M. Thorne (2003), Relativistic electron pitch angle scattering by electromagnetic ion cyclotron waves during geomagnetic storms, *J. Geophys. Res.*, 108(A4), 1143, doi:10.1029/2002JA009489.

Suvorova, A., A. Dmitriev, J.-K. Chao, M. Thomsen, and Y.-H. Yang (2005), Necessary conditions for geosynchronous magnetopause crossings, *J. Geophys. Res.*, 110(A1), A01206, doi:10.1029/2003JA010079.

Takahashi, K., and A. Y. Ukhorskiy (2008), Timing analysis of the relationship between solar wind parameters and geosynchronous Pc5 amplitude, *J. Geophys. Res.*, 113(A12), A12204, doi:10.1029/2008JA013327.

Thomsen, M. F. (2004), Why *Kp* is such a good measure of magnetospheric convection, *Space Weather*, 2(11), S11004, doi:10.1029/2004SW000089.

Thomsen, M. F., D. J. McComas, G. D. Reeves, and L. A. Weiss (1996), An observational test of the Tsyganenko (T89a) model of the magnetospheric field, *J. Geophys. Res.*, 101(A11), 24,827–24,836.

Thomsen, M. F., E. Noveroske, J. E. Borovsky, and D. J. McComas (1999), Calculating the moments from measurements by the Los Alamos magnetospheric plasma analyzer, *LA Rep. LA-13566-MS*, Los Alamos Natl. Lab., Los Alamos, N. M.

Thorne, R. B., and C. F. Kennel (1971), Relativistic electron precipitation during magnetic storm main phase, *J. Geophys. Res.*, 76(19), 4446–4453.

Troshichev, O. A., V. G. Andrezen, S. Vennerstrøm, and E. Friis-Christensen (1988), Magnetic activity in the polar cap – A new index, *Planet. Space Sci.*, 11, 1095–1102.

Troshichev, O. A., H. Hayakawa, A. Matsuoka, T. Mukai, and K. Tsuruda (1996), Cross-polar cap diameter and voltage as a function of PC index and interplanetary quantities, *J. Geophys. Res.*, 101(A6), 13,429–13,435.

Troshichev, O. A., R. Y. Lukianova, V. O. Papitashvili, F. J. Rich, and O. Rasmussen (2000), Polar cap index (PC) as a proxy for ionospheric electric field in the near-pole region, *Geophys. Res. Lett.*, 27(23), 3809–3812, doi:10.1029/2000GL003756.

Tsurutani, B. T., and W. D. Gonzalez (1997), The interplanetary causes of magnetic storms: A review, in *Magnetic Storms*, edited by B. T. Tsurutani et al., AGU, Washington, D. C.

Tsurutani, B. T., W. D. Gonzalez, F. Tang, S. I. Akasofu, and E. J. Smith (1988), Origin of interplanetary southward magnetic fields responsible for major magnetic storms near solar maximum (1978–1979), *J. Geophys. Res.*, 93(A8), 8519–8531.

Tsurutani, B. T., W. D. Gonzalez, A. L. C. Gonzalez, F. Tang, J. K. Arballo, and M. Okada (1995), Interplanetary origin of geomagnetic activity in the declining phase of the solar cycle, *J. Geophys. Res.*, 100(A11), 21,717–21,733.

Tsurutani, B. T., W. D. Gonzalez, Y. Kamide, C. M. Ho, G. S. Lakhina, J. K. Arballo, R. M. Thorne, J. S. Pickett, and R. A. Howard (1999), The interplanetary causes of magnetic storms, HILDCAAs and viscous interaction, *Phys. Chem. Earth C Sol. Terr. Planet. Sci.*, 24, 93–99.

Tsurutani, B. T., et al. (2006a), Corotating solar wind streams and recurrent geomagnetic activity: A review, *J. Geophys. Res.*, 111(A7), A07S01, doi:10.1029/2005JA011273.

Tsurutani, B., R. McPherron, W. Gonzalez, G. Lu, J. H. A. Sobral, and N. Gopalswamy (Eds.) (2006b), *Recurrent Magnetic Storms: Corotating Solar Wind Streams*, AGU, Washington, D. C.

Tsyganenko, N. A. (1996), Effects of the solar wind conditions on the global magnetospheric configuration as deduced from data-based field models, in *Proceedings of the Third International Conference on Substorms*, *Eur. Space Agency Spec. Publ.*, ESA SP-389, p. 181.

Tsyganenko, N. A., H. J. Singer, and J. C. Kasper (2003), Storm-time distortion of the inner magnetosphere: How severe can it get?, *J. Geophys. Res.*, 108(A5), 1209, doi:10.1029/2002JA009808.

Turner, N. E., D. N. Baker, T. I. Pulkkinen, and R. L. McPherron (2000), Evaluation of the tail current contribution to *Dst*, *J. Geophys. Res.*, 105(A3), 5431–5439.

Turner, N. E., E. J. Mitchell, D. J. Knipp, and B. A. Emery (2006), Energetics of magnetic storms driven by corotating interaction regions: A study of geoeffectiveness, in *Recurrent Magnetic Storms*, edited by B. Tsurutani et al., p. 113, AGU, Washington, D. C.

Turner, N. E., W. D. Cramer, S. K. Earles, and B. A. Emery (2009), Geoefficiency and energy partitioning in CIR-driven and CME-driven storms, *J. Atmos. Sol. Terr. Phys.*, 71, 1023–1031.

Ukhorskiy, A. Y., B. J. Anderson, P. C. Brandt, and N. A. Tsyganenko (2006), Storm time evolution of the outer radiation belt: Transport and losses, *J. Geophys. Res.*, 111(A11), A11S03, doi:10.1029/2006JA011690.

Vassiliadis, D., A. J. Klimas, and D. N. Baker (1999), Models of D_{st} geomagnetic activity and of its coupling to solar wind parameters, *Phys. Chem. Earth (C)*, 24, 107–112.

Vasyliunas, V. M. (2004), Comparitive magnetospheres: Lessons for Earth, *Adv. Space Res.*, 33, 2113–2120.

Villante, U., and M. Piersanti (2008), An analysis of sudden impulses at geosynchronous orbit, *J. Geophys. Res.*, 113(A8), A08213, doi:10.1029/2008JA013028.

West, H. I., R. M. Buck, and J. R. Walton (1972), Shadowing of electron azimuthal-drift motions near the noon magnetopause, *Nature Phys. Sci.*, 240, 6.

West, H. I., R. M. Buck, and J. R. Walton (1973), Electron pitch angle distributions throughout the magnetosphere as observed on Ogo 5, *J. Geophys. Res.*, 78(7), 1064–1081.

Wing, S., and D. G. Sibeck (1997), Effects of interplanetary magnetic field *z* component and the solar wind dynamic pressure on the geosynchronous magnetic field, *J. Geophys. Res.*, 102(A4), 7207–7216.

Wrenn, G. L., and A. J. Sims (1996), Internal charging in the outer zone and operational anomalies, in *Radiation Belts: Models and Standards*, edited by J. F. Lemaire, D. Heynderickx, and D. N. Baker, p. 275, AGU, Washington, D. C.

Wrenn, G. L., D. J. Rodgers, and K. A. Ryden (2002), A solar cycle of spacecraft anomalies due to internal charging, *Ann. Geophys.*, 20, 953–956.

Yermolaev, Y. U., and M. Y. Yermolaev (2002), Statistical relationships between solar, interplanetary, and geomagnetospheric disturbances, 1976–2000, *Cosmic Res.*, 40(1), 1–14.

Yermolaev, Y. I., M. Y. Yermolaev, I. G. Lodkina, and N. S. Nikolaeva (2007), Statistical investigation of heliospheric conditions resulting in magnetic storms, *Cosmic Res.*, 45, 1–8.

Zhang, J. C., M. W. Liemohn, J. U. Kozyra, M. F. Thomsen, H. A. Elliott, and J. M. Weygand (2006), A statistical comparison of solar wind sources of moderate and intense geomagnetic storms at solar minimum and maximum, *J. Geophys. Res.*, 111(A1), A01104, doi:10.1029/2005JA011065.

J. E. Borovsky, Space Science and Applications, Los Alamos National Laboratory, MS D466, Los Alamos, NM 87545, USA. (jborovsky@lanl.gov)

M. H. Denton, Communications Systems, Lancaster University, Lancaster, Lancashire LA1 4WA, UK.